Stability and crack nucleation in variational phase-field models of fracture: effects of length-scales and stress multi-axiality

Camilla Zolesi, Corrado Maurini

Stability and crack nucleation in variational phase-field models of fracture: effects of length-scales and stress multi-axiality

Camilla Zolesi[a], Corrado Maurini[a]

[a]*Institut Jean Le Rond d'Alembert, Sorbonne University and CNRS, UMR 7190, Paris, 75252, France*

Abstract

We study the problem of nucleation of cracks in gradient damage models used as regularized phase-field model of fracture. We consider specific phase-field models with a linear softening response, with possibly different softening parameters for the spherical and the deviatoric deformation modes. The softening parameters enable the independent adjustment of toughness, stiffness, and peak stress, irrespective of the regularization length-scale. This capability effectively establishes a cohesive-like phase-field model. We exploit a variational formulation to examine the crack nucleation conditions, characterizing stable solutions as directional local minima of the total energy functional. Our analytical results in one dimension reveal intricate scale effects, which emerge from the interaction between the structural scale, the material's cohesive length-scale, and the regularization length. We establish conditions on the material parameters that determine whether the crack nucleation behavior is brittle-like or cohesive-like, offering a clear and classical energetic interpretation for these conditions. These factors influence the conditions for crack nucleation. We establish conditions on the material parameters that determine whether the behavior is brittle-like or cohesive-like, offering a clear and classical energetic interpretation for these conditions. In a two-dimensional setting, we demonstrate that crack nucleation under multi-axial loading presents greater complexity. We show that the volumetric deformation mode can remain stable in the softening regime, regardless of the length-scale effects. Our findings deepen the understanding of the intricate relationship between material softening, the regularization length-scale, the loading mode, and strength. This sheds new light on the numerical results of phase-field models, where solutions with diffused and localized damage can compete.

Keywords: Fracture, gradient damage, softening, phase-field, stability, strength, crack nucleation

1. Introduction

Phase-field models of fracture are simple and effective tools to reproduce numerically the propagation and nucleation of complex crack networks. The classical version of phase-field model, originally obtained as a variational regularization of brittle fracture models (Bourdin et al., 2000), converges asymptotically to Griffith models when the regularization length goes to zero (Ambrosio and Tortorelli, 1990). This property guarantees the conditions for the propagation of pre-existing cracks to be consistent with sharp interface Griffith fracture models. In these models, the energy dissipated in a unit surface crack, the fracture toughness G_c, is a well-defined quantity. Phase field model also produce the nucleation of cracks with or without pre-existing singularities. Yet, the conditions for crack nucleation are subtler and currently object of a debate (Tanné et al., 2018; Kumar and Lopez-Pamies, 2021). The nucleation

threshold cannot be directly related to the sharp interface Griffith model, for which crack nucleation is an issue (Bourdin et al., 2008), and requires the identification of an additional material property, the strength σ_c, roughly defined as the critical stress for crack nucleation.

The current understanding of crack nucleation in phase-field models comes from their interpretation as gradient damage models with a regularization length-scale ℓ (Frémond and Nedjar, 1996; Lorentz and Andrieux, 2003; Lorentz and Benallal, 2005; Amor et al., 2009). Crack nucleation is the outcome of a structural instability in the nonlinear damage evolution (Pham et al., 2011a,b). The instability of solutions with vanishing or diffuse damage leads to the localization of damage in thin bands of width proportional to ℓ. The bands stand for the smeared representation of cracks. In this framework, the regularization length ℓ is set in order to retrieve the phenomenological strength σ_c. Hence, ℓ is linked to the Irwin length through σ_c, the fracture toughness G_c, and the material's Young modulus E_0. We define the Irwin length, also referred to as the cohesive length-scale, as (Irwin, 1958; Griffith, 1921)

$$\ell_{\text{ch}} = \frac{2G_c E_0}{\sigma_c^2}. \tag{1}$$

It is the ratio between the crack energy per unit area ($\sim G_c$) and the elastic energy per unit volume at failure ($\sim \sigma_c^2/2E$). Considering a one-dimensional traction problem, Pham et al. (2011b,a) show that, for bars that are sufficient long with respect to the regularization length-scale, the peak stress of the local material response coincides with the strength. At the peak stress, the solution with diffused damage becomes unstable, hence the damage and the deformation localize in a crack band. The energy dissipated in the localized solution defines the fracture toughness G_c. Tanné et al. (2018) and Bourdin et al. (2014) extend this reasoning to more complex two and three-dimensional cases, showing the ability of phase-field models to faithfully retrieving crack nucleation in notched or nominally homogeneous structures under dominant traction-like loading states. The theoretical (Sicsic et al., 2014) and numerical (León Baldelli and Maurini, 2021) stability analysis explains the morphogenesis of the emerging crack patterns by looking at the shapes of the lower energy instability modes. This approach provides a consistent macroscopic understanding of crack nucleation as a structural instability of a non-linear softening continuum. The main limitation are that (i) in the multi-dimensional setting the results are consistent only for the case of almost uniaxial stress states, (ii) the regularization length-scale ℓ is directly related to the cohesive length ℓ_{ch} and cannot be tuned independently of the material strength, toughness, and stiffness.

To decouple the cohesive length-scale ℓ_{ch} from the regularization length ℓ, Lorentz et al. (2012) introduced an additional parameter that modulates the softening of the local material behavior (see also Lorentz and Benallal, 2005). They obtain a phase-field model with an equivalent cohesive behavior, where the peak stress and the toughness G_c are independent of the regularization length for ℓ sufficiently small (Lorentz et al., 2011). Alessi et al. (2014a) use damage models with similar parametric softening modulation to investigate the coupling between damage and plasticity, an effort which is further pursed is several additional works (see e.g. Alessi et al., 2018; Talamini et al., 2021). Wu and Nguyen (2018) further develop this idea, naming this class of models as "length-scale insensitive" phase-field models. Conti et al. (2016, 2024); Larsen (2023); Feng and Li (2022) propose alternative interesting approaches to obtain cohesive phase-field models with independent strength and toughness.

Modelling crack nucleation under multi-axial loadings requires accounting for the tensorial nature of the stress. The maximal allowable stress before crack nucleation depends on the loading mode. The strength is not a single scalar value but a surface in the stress space delimiting the domain of admissible stress states. As discussed in Amor et al. (2009), classical

formulation of phase-field fracture models are not able to independently tune the strength under uniaxial traction, compression, or pure shear. Kumar and Lopez-Pamies (2021) spotlight this drawback. They argue that the energetic argument at the basis of the definition (1) cannot be applied for almost incompressible elastic materials, where, for isotropic stress states, the bulk modulus representing the stiffness tends to infinite while σ_c stays finite. They conclude that crack nucleation cannot be the result of an energy criterion, because the elastic energy is vanishing in the incompressible limit. Hence, they propose a non-variational phase-field fracture theory, introducing the strength criterion as an additional ingredient in the phase-field equation. To fit the experimental strength, they introduce an additional ad-hoc driving force in the phase-field equation, whose mechanical and thermodynamical origin remains to be specified.

The use of phase-field models with an equivalent cohesive behavior comes as an appealing tool to overcome the limitations of classical phase-field model on crack nucleation under multi-axial loading (Lorentz et al., 2011; **?**; Conti et al., 2016; Wu and Nguyen, 2018; Feng and Li, 2022). As it will detailed later, at the first sight, the softening modulation of the so-called "length-scale insensitive" models adds the flexibility to introduce different peak stress and cohesive behaviors depending on the loading mode. Exploiting suitable energy decompositions, one could generate model with adjustable elastic limits and peak loads under traction and shear, or compression, expanding on the ideas presented in (Amor et al., 2009; Lorenzis and Maurini, 2021; Vicentini et al., 2024).

Most of the literature assumes that the strength of the phase-field model is directly related to the peak stress of the local material behavior, and that crack nucleates as soon as the model enter the softening regime. In this paper, we show that the nucleation conditions in variational gradient damage models are more complex. We present an in-depth analysis of the conditions for crack nucleation under multi-axial loading when considering models with parametric stiffness modulation. First, we show that the identification of the strength with the nominal peak load of the local material behavior is abusive, especially when using cohesive-like models with softening modulation. Our theoretical and numerical stability analysis discloses a non-trivial interplay between the material softening, the regularization lenght-scale, the loading mode, and the strength, bringing new insights for the understanding of the numerical outcomes of phase-field models, where solutions with diffused and localized damage can compete. We characterize the crack nucleation conditions for the phase-field models with selective stiffness modulation in the deviatoric and spherical deformation modes and show that: (i) the stiffness modulation of nominally "length-scale insensitive" phase-field models implies non-trivial scale effects between the structural scale L, the material cohesive length-scale ℓ_{ch}, and the regularization length ℓ, that has important consequence on the crack nucleation conditions and the effective strength; (ii) nucleating crack under isotropic loading is intrinsically more difficult that in the deviatoric case; the volumetric deformation mode can be stable in the softening regime independently of the length-scale effects. We further relate the two findings above with classical energetic and stress conditions for crack nucleation (Irwin, 1958; Griffith, 1921) and material stability conditions for non-linear dissipative continua (Hill, 1958; Ball, 1980; Nguyen and Triantafyllidis, 1989; Benallal et al., 1993; Bigoni, 2012).

The paper is organised as follows. Section 2 introduces the modelling framework and the specific class of phase-field models considered in this work. Section 3 presents a theoretical stability analysis in a one-dimensional setting when considering models with stiffness modulation, showing non-trivial scale-effects that affect the crack nucleation condition and the effective strength. We also discuss in passing the case of almost inextensible bars with finite strength and toughness. Section 4 considers the case of multiaxial loadings. Section 5

concludes the paper.

Throughout this paper, we consider a geometrically linear model and quasi-static conditions. We denote by $\mathbf{u}$ the n-dimensional displacement field, by $\boldsymbol{\varepsilon} = \mathrm{sym}(\nabla \mathbf{u})$ the linearized strain tensor, and by $\boldsymbol{\sigma}$ the Cauchy stress, where $n = 2$ in two-dimensional elasticity and $n = 3$ in three dimensions. We will use the notation $\boldsymbol{\varepsilon}^{\mathrm{dev}}$ and $|\boldsymbol{\varepsilon}| := \sqrt{\boldsymbol{\varepsilon} \cdot \boldsymbol{\varepsilon}}$ for the deviatoric part and the Frobenius norm of tensors, and $f^+ := (f + |f|)/2$ or $f^- := (|f| - f)/2$ for the positive or negative part of a function f. Denoting by E_0, ν_0, λ_0 and μ_0 the Young modulus, Poisson ratio and Lamé's coefficients of the undamaged isotropic material, we recall the following basic relations, where $n = 2$ for in two dimensions and $n = 3$ in three dimensions:

$$\mu_0 := \mu(0) = \frac{E_0}{2(1+\nu_0)}, \quad \kappa_0 := \kappa(0) = \lambda_0 + \frac{2\mu_0}{n} = \frac{E_0}{n[1-(n-1)\nu_0]}. \tag{2}$$

2. Variational gradient damage models of brittle fracture with softening modulation

2.1. Material model: selective linear-softening (S-LS)

We consider a phase-field model with softening modulation featuring the following strain energy density

$$W(\boldsymbol{\varepsilon}, \alpha, \nabla\alpha) = \frac{\kappa_0}{2}\mathrm{tr}^-(\boldsymbol{\varepsilon})^2 + \frac{\kappa(\alpha)}{2}\mathrm{tr}^+(\boldsymbol{\varepsilon})^2 + \mu(\alpha)\,|\boldsymbol{\varepsilon}^{\mathrm{dev}}|^2 + w_1(w(\alpha) + \ell^2|\nabla\alpha|^2), \tag{3}$$

where $\boldsymbol{\varepsilon}$ is the linearized strain tensor, α is a scalar damage parameter, $\nabla\alpha$ its spatial gradient. The constants w_1 and ℓ represent the energy required to fully damage a volume element in a homogeneous process and the regularization length, respectively. The function $\kappa(\alpha)$ and $\mu(\alpha)$ are the volumetric and deviatoric stiffness constants, whilst $w(\alpha)$ gives the dependence of the specific dissipation per unit volume on the damage variable. The relationship between the Cauchy stress $\boldsymbol{\sigma}$ and the strain is given by

$$\boldsymbol{\sigma} = \frac{\partial W}{\partial \boldsymbol{\varepsilon}} = \left(\kappa_0\,\mathrm{tr}^-(\boldsymbol{\varepsilon}) + \kappa(\alpha)\,\mathrm{tr}^+(\boldsymbol{\varepsilon})\right)\mathbf{I}_n + 2\mu(\alpha)\,\boldsymbol{\varepsilon}^{\mathrm{dev}},$$

where $\mathbf{I}_n$ is the n-dimensional identity matrix. Here and henceforth, we denote by

$$p := \frac{\mathrm{tr}(\boldsymbol{\sigma})}{n} = \kappa_0\,\mathrm{tr}^-(\boldsymbol{\varepsilon}) + \kappa(\alpha)\,\mathrm{tr}^+(\boldsymbol{\varepsilon}), \qquad \tau := \frac{|\boldsymbol{\sigma}^{\mathrm{dev}}|}{\sqrt{2}} = \sqrt{2}\,\mu(\alpha)\,|\boldsymbol{\varepsilon}^{\mathrm{dev}}| \tag{4}$$

the pressure and the shear stress, that are used as norms of the volumetric and deviatoric part of the stress.

We consider the material model characterized by the following degradation and dissipation functions

$$\kappa(\alpha) := \frac{1-w(\alpha)}{1+(\gamma_\kappa-1)\,w(\alpha)}\kappa_0, \quad \mu(\alpha) := \frac{1-w(\alpha)}{1+(\gamma_\mu-1)\,w(\alpha)}\mu_0, \quad w(\alpha) := 1-(1-\alpha)^2. \tag{5}$$

This model was originally introduced in a one-dimensional context by Alessi et al. (2014b). Here, we extend it to a spheric-deviatoric decomposition of the strain energy density, including a selective softening parameter, γ_κ and γ_μ, for the spherical and deviatoric contributions, respectively. Models of the same type, without the spheric-deviatoric decomposition and with a different $w(\alpha)$, have been introduced by Lorentz et al. (2011) on damage approximation of cohesive fracture models and by Lorentz and Benallal (2005). They are also considered in

the discussion of Wu and Nguyen (2018) on length-scale insensitive phase-field models. The specific choice of the function $w(\alpha)$ adopted here allows for a complete analytical solution of the one-dimensional traction problem (Alessi et al., 2014b).

Here and henceforth, we will denote the model (5) as the selective linear-softening model (S-LS). As we will show later, the homogeneous stress-strain response of this model is characterized by a linear softening regime with a constant softening slope determined by γ_κ and γ_μ for the purely spherical and purely deviatoric loading modes, respectively.

2.2. Time-continuous variational formulation of the evolution problem and state-stability

We consider a body $\Omega \subset \mathbb{R}^n$ loaded by a time-dependent imposed displacement $\bar{\mathbf{u}}_t$ on the part $\partial_u\Omega$ of the boundary. For the sake of simplicity, we assume here that body and boundary forces on $\partial\Omega \setminus \partial_u\Omega$ vanish. We introduce the total energy functional

$$\mathcal{E}(\mathbf{u},\alpha) := \int_\Omega W(\boldsymbol{\varepsilon}(\mathbf{u}(\mathbf{x})), \alpha(\mathbf{x}), \nabla\alpha(\mathbf{x}))\,\mathrm{d}\Omega \tag{6}$$

and the following functional space of admissible displacement and damage fields at time t:

$$\mathcal{C}_t := \{\mathbf{u} \in H^1(\Omega;\mathbb{R}^n) : \mathbf{u} = \bar{\mathbf{u}}_t \text{ on } \partial_u\Omega\}, \tag{7}$$

$$\mathcal{D}_t(\alpha_t) := \{\alpha \in H^1(\Omega;\mathbb{R}) : \alpha = \bar{\alpha}_t \text{ on } \partial_\alpha\Omega,\ \alpha_t \le \alpha(x) < 1\}. \tag{8}$$

where α_t is the current damage field and $H^1(\Omega;\mathbb{R}^n)$ denotes the Sobolev space of $\mathbb{R}^n$-valued functions defined in Ω with square integrable first derivatives. The set of the admissible damage fields at time t is an affine cone, because of the unilateral constraint on the damage variable, that enforces the damage irreversibility condition[1]. It may include additional Dirichlet boundary condition imposing a damage field $\bar{\alpha}_t$ on a part $\partial_\alpha\Omega$ of the boundary.

We define quasi-static evolutions according to the variational approach to rate-independent processes (see e.g. Mielke, 2005). Given an initial state at time $t = 0$, smooth-in-time quasi-static evolution $(\mathbf{u}_t, \alpha_t) \in \mathcal{C}_t \times \mathcal{D}(\alpha_t)$ must satisfy, at each time t, the following conditions:

- Irreversibility (IR):
$$\dot{\alpha}_t \ge 0; \tag{9}$$

- State-stablity (SS): the solution should be a unilateral local mininum of the energy, in the following directional sense:
$$\forall(\hat{\mathbf{u}},\hat{\alpha}) \in \mathcal{C}_t \times \mathcal{D}(\alpha_t),\ \exists \bar{h} > 0 :\ \forall h \in [0,\bar{h}] \quad \mathcal{E}(\mathbf{u}_t + h(\hat{\mathbf{u}} - \mathbf{u}_t), \alpha_t + h(\hat{\alpha} - \alpha_t)) - \mathcal{E}(\mathbf{u}_t,\alpha_t) \ge 0; \tag{10}$$

- Energy balance (EB):
$$\mathcal{E}'(\mathbf{u}_t,\alpha_t)(\mathbf{0},\dot{\alpha}_t) = 0 \quad \Leftrightarrow \quad \int_\Omega \left(\frac{\partial W(\boldsymbol{\varepsilon}(\mathbf{u}_t), \alpha_t, \nabla\alpha_t)}{\partial\alpha}\,\dot{\alpha}_t + 2\ell^2 \nabla\alpha_t \cdot \nabla\dot{\alpha}_t \right) \mathrm{d}\Omega = 0. \tag{11}$$

[1]Wherever $\alpha = 1$, the functional spaces are less regular. One should allow for discontinuities of the displacement field and the admissible damage variation β should vanish.

where, here and henceforth,

$$\mathcal{E}'(\mathbf{u},\alpha)(\mathbf{v},\beta) := \frac{d}{dh}\mathcal{E}(\mathbf{u}+h\mathbf{v},\alpha+h\beta)\Big|_{h=0}, \quad \mathcal{E}''(\mathbf{u},\alpha)(\mathbf{v},\beta) := \frac{d^2}{dh^2}\mathcal{E}(\mathbf{u}+h\mathbf{v},\alpha+h\beta)\Big|_{h=0,}$$

denotes the first and second directional derivatives of the functional $\mathcal{E}(\mathbf{u},\alpha)$ in the direction $(\mathbf{v},\beta)$. For further details on the evolution principle and the equivalence between the condition (11) and the energy balance, we refer the reader to Marigo et al. (2016); Pham et al. (2011a,b). In the SS condition, the spaces of admissible variations from a damaged state with $\sup_\Omega \alpha_t(x) < 1$ are :

$$\mathcal{C}_0 := \{\mathbf{v} \in H^1(\Omega;\mathbb{R}^n) : \mathbf{v} = \mathbf{0} \text{ on } \partial_u\Omega\}, \quad \mathcal{D}_0^+ := \{\beta \in H^1(\Omega;\mathbb{R}) : \beta = 0 \text{ on } \partial_\alpha\Omega,\ \beta(x) \geq 0\}. \tag{12}$$

The directional Taylor expansion of the energy increment with respect to the increment amplitude h in (10) reads as follows:

$$\mathcal{E}(\mathbf{u}_t + h\mathbf{v}, \alpha_t + h\beta) - \mathcal{E}(\mathbf{u}_t,\alpha_t) = h\,\mathcal{E}'(\mathbf{u}_t,\alpha_t)(\mathbf{v},\beta) + \frac{h^2}{2}\,\mathcal{E}''(\mathbf{u}_t,\alpha_t)(\mathbf{v},\beta) + \mathcal{O}(h^2). \tag{13}$$

Imposing the first term of the energy increment in (10) non-negative gives the following first-order necessary stability condition (FOSS):

$$\mathcal{E}_t'(\mathbf{u}_t,\alpha_t)(\mathbf{v},\beta) = \mathcal{E}_t'(\mathbf{u}_t,\alpha_t)(\mathbf{v},0) + \mathcal{E}_t'(\mathbf{u}_t,\alpha_t)(\mathbf{0},\beta) \geq 0, \quad \forall (\mathbf{v},\beta) \in \mathcal{C}_0 \times \mathcal{D}_0^+. \tag{14}$$

The arbitrariness of the FOSS condition with respect to $\mathbf{v}$ for $\beta = 0$ gives, after integration by parts and localization arguments, the following equilibrium equilibrium condition

$$\operatorname{div}\boldsymbol{\sigma} = \mathbf{0} \text{ on } \Omega, \quad \boldsymbol{\sigma}\,\mathbf{n} = \text{ on } \partial_N\Omega. \tag{15}$$

For $\alpha_t < 1$, the combination of the irreversibility, energy balance, and FOSS condition with respect to β for $\mathbf{v} = 0$, gives the following damage criterion in the form of Karush-Kuhn-Tucker complementary conditions:

$$\dot\alpha_t \geq 0, \qquad \frac{\partial W}{\partial \alpha} - 2\ell^2 w_1 \Delta\alpha_t \geq 0, \qquad \left(\frac{\partial W}{\partial \alpha} - 2\ell^2 w_1 \Delta\alpha_t\right)\dot\alpha_t = 0 \qquad \text{on } \Omega, \tag{16a}$$

$$\dot\alpha_t \geq 0, \qquad \nabla\alpha_t \cdot \mathbf{n} \geq 0, \qquad (\nabla\alpha_t \cdot \mathbf{n})\,\dot\alpha_t = 0 \qquad \text{on } \partial\Omega, \tag{16b}$$

where $\mathbf{n}$ is the outer unit normal to the boundary and $\Delta\alpha$ denotes the Laplacian of the damage field. The optimality conditions (16) does not apply wherever $\alpha_t(x) = 1$, where the upper bounds in (12) is active and the admissible damage variations must vanish.

Establishing a sufficient condition for state-stability requires to study the sign of the second-order term of the expansion (13) along the directions $(\mathbf{v},\beta)$ where the first-order terms vanishes. These directions span the space where the irreversibility constraint is not-strongly active:

$$\mathcal{N}_0^+ := \{(\mathbf{v},\beta) \in \mathcal{C}_0 \times \mathcal{D}_0^+ : \quad \mathcal{E}'(\mathbf{u}_t,\alpha_t)(\mathbf{v},\beta) = 0\}. \tag{17}$$

If the second derivative of the energy is positive for along all the non-vanishing directions in $\mathcal{N}_0^+$, a state verifying the FOSS condition is state-stable. We can conclude with the following sufficient condition for state-stability.

Second-Order State-Stability condition (SOSS). A state $(\mathbf{u}_t,\alpha_t)$ verifying the equilibrium (15) and damage criterion (16) is state-stable if

$$\mathcal{E}_t''(\mathbf{u}_t,\alpha_t)(\mathbf{v},\beta) > 0, \quad \forall (\mathbf{v},\beta) \in \mathcal{N}_0^+, \quad (\mathbf{v},\beta) \neq (\mathbf{0},0). \tag{18}$$

2.3. Time-discrete variational formulation of the evolution problem and incremental-stability

The numerical solution of the problem requires its time discretisation. Denoting by $(\mathbf{u}_i, \alpha_i)$ the solution at time t_i and $\Delta t_i = t_i - t_{i-1}$ the time increment, an incremental variational principle defines the time-discrete quasi-static evolution of the damage model. Given an initial state $(\mathbf{u}_0, \alpha_0)$, the solution $(\mathbf{u}_i, \alpha_i) \in \mathcal{C}_i \times \mathcal{D}(\alpha_{i-1})$ must satisfy the following

- Incremental-Stability (IS) condition.

$$\forall (\hat{\mathbf{u}}, \hat{\alpha}) \in \mathcal{C}_i \times \mathcal{D}_i(\alpha_{i-1}),\ \exists \bar{h} > 0 :\ \forall h \in [0, \bar{h}] \quad \mathcal{E}(\mathbf{u} + h(\hat{\mathbf{u}} - \mathbf{u}), \alpha + h(\hat{\alpha} - \alpha)) - \mathcal{E}(\mathbf{u}, \alpha) \geq 0. \tag{19}$$

The first-order Taylor expansion gives the First-Order Incremental-Stability (IS-FO) condition:

$$(\mathbf{u}_i, \alpha_i) \in \mathcal{C}_i \times \mathcal{D}_i(\alpha_{i-1}) : \quad \mathcal{E}'(\mathbf{u}_i, \alpha_i)(\hat{\mathbf{u}}_i - \mathbf{u}, \hat{\alpha}_i - \alpha) \geq 0, \quad \forall (\hat{\mathbf{u}}, \hat{\alpha}) \in \mathcal{C}_i \times \mathcal{D}_i(\alpha_{i-1}), \tag{20}$$

The subtle, but relevant, difference between the SS condition (10) and the IS condition (20) is on the irreversibility. On one hand, in the definition of the space $\mathcal{D}_i(\alpha_{i-1})$ of IS, the irreversibility condition is with respect to the damage field at the previous time step α_{i-1}. On the other hand, in the definition of the space $\mathcal{D}_t(\alpha_t)$, it is with respect to the damage field at the current time $\alpha_i = \alpha_{t_i}$. This implies that admissible damage variations are always non-negatives in SS, whilst they can be positive or negative in IS wherever the damage evolves, *i.e.* $\alpha_i > \alpha_{i-1}$. Since the first derivative is linear with respect to the variation, in the directions where positive and negative variations are admissible, the first derivative must be equal to zero. Hence, the fact that the sign of the admissible variation can also be negative implies that the sole IS condition implies the full set of discrete KKT complementary conditions without the need to consider the energy balance (11), as in the case of the SS condition, see León Baldelli and Maurini (2021) for further details.

As for state-stability, establishing a sufficient condition for the incremental-stability (20) requires to check the sign of the second-order terms of the series expansion of the energy along the directions where the first-order terms vanishes. These directions span the space where the irreversibility constraint $\alpha \geq \alpha_{i-1}$ is not-strongly active:

$$\mathcal{N}_0 := \{(\mathbf{v}, \beta) \in \mathcal{C}_0 \times \mathcal{D}_0 : \quad \mathcal{E}'(\mathbf{u}_t, \alpha_t)(\mathbf{v}, \beta) = 0\}. \tag{21}$$

We obtain the following sufficient condition for incremental-stability.

Second-Order Increment-Stability condition (SOIS). A state $(\mathbf{u}_t, \alpha_t)$ verifying the equilibrium (15) and damage criterion (16) is incrementally-stable if

$$\mathcal{E}_i''(\mathbf{u}_i, \alpha_i)(\mathbf{v}, \beta) > 0, \quad \forall (\mathbf{v}, \beta) \in \mathcal{N}_0, \quad (\mathbf{v}, \beta) \neq (\mathbf{0}, 0). \tag{22}$$

Differently from the state-stability case, the admissible variations are not restricted to be non-negative. The condition of positive-definiteness of the second-derivative on $\mathcal{N}_0$ is stronger than its positive-definiteness on its subset $\mathcal{N}_0^+ \subseteq \mathcal{N}_0$. This means that the IS implies SS, but not viceversa. The SOIS condition (22) is a sufficient condition for incremental-stability, but it is not necessary. A sufficient condition for incremental-instability (IU) is that there exists a direction along which the second derivative is negative in the space of not-active constraint:

$$\mathcal{N}_0^{\mathrm{na}} := \{(\mathbf{v}, \beta) \in \mathcal{N}_0 : \alpha_i > \alpha_{i-1}\} \subseteq \mathcal{N}_0. \tag{23}$$

Note that the IS and SS conditions, corresponds to the non-bifurcation (or uniqueness) and stability conditions in the works of Pham et al. (2011a,b) and other classical works on the stability and bifurcation analysis of rate-independent problems (see e.g. Benallal et al., 1993; Nguyen, 1993; Petryk, 1993; Potier-Ferry, 1985; Fedelich and Ehrlacher, 1997), as discussed in León Baldelli and Maurini (2021).

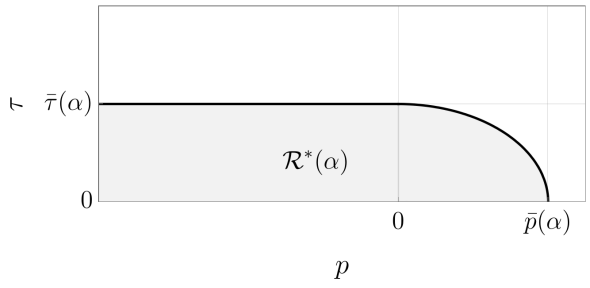

Figure 1: Domain of admissible stress $\mathcal{R}^*(\alpha)$ for homgeneous stress states, see equation (24b).

2.4. Admissible stress and strain domains for homogeneous states

For homogeneous states $\Delta\alpha = 0$, the damage criterion (16) implies that the admissible strains and the stresses must lies in the following elastic domains, parametrized by the damage level α:

$$\mathcal{R}(\alpha) := \left\{\boldsymbol{\varepsilon} : -\left(\frac{\kappa'(\alpha)}{2}\,\mathrm{tr}^+(\boldsymbol{\varepsilon})^2 + \mu'(\alpha)\,|\boldsymbol{\varepsilon}^{\mathrm{dev}}|^2\right) \leq w_1\, w'(\alpha)\right\}, \tag{24a}$$

$$\mathcal{R}^*(\alpha) := \left\{\boldsymbol{\sigma} : s'_\kappa(\alpha)\frac{(p^+)^2}{2} + s'_\mu(\alpha)\,\frac{\tau^2}{2} \leq w_1\, w'(\alpha)\right\}, \tag{24b}$$

where $s_\kappa(\alpha) := 1/\kappa(\alpha)$ and $s_\mu(\alpha) := 1/\mu(\alpha)$ are the compliance modulation functions, with the pressure and the shear stress p and τ defined in (4). Moreover, because of the complementary conditions (16) the damage can evolve only if the stress and the strain are on the boundary of the elastic domains above. For the specific constitutive model (5), the strain and stress domains writes as, respectively:

$$\mathcal{R}(\alpha) \equiv \left\{\boldsymbol{\varepsilon} : \quad \frac{\mathrm{tr}^+(\boldsymbol{\varepsilon})^2}{\bar{\varepsilon}_\kappa(\alpha)^2} + \frac{2|\boldsymbol{\varepsilon}^{\mathrm{dev}}|^2}{\bar{\varepsilon}_\mu(\alpha)^2} \leq 1\right\}, \qquad \mathcal{R}^*(\alpha) \equiv \left\{\boldsymbol{\sigma} : \quad \frac{(p^+)^2}{\bar{p}(\alpha)^2} + \frac{\tau^2}{\bar{\tau}(\alpha)^2} \leq 1\right\}, \tag{25}$$

where

$$\bar{\varepsilon}_\kappa(\alpha) = \sqrt{\frac{2w_1}{\gamma_\kappa\kappa_0}}(1 + (\gamma_\kappa - 1)w(\alpha)), \quad \bar{\varepsilon}_\mu(\alpha) = \sqrt{\frac{2w_1}{\gamma_\mu\mu_0}}(1 + (\gamma_\mu - 1)w(\alpha)), \tag{26}$$

and

$$\bar{p}(\alpha) = \sqrt{\frac{2\kappa_0 w_1}{\gamma_\kappa}}(1 - w(\alpha)), \qquad \bar{\tau}(\alpha) = \sqrt{\frac{2\mu_0 w_1}{\gamma_\mu}}(1 - w(\alpha)). \tag{27}$$

Figure 1 reports the domain of admissible stress in the (p,τ) plane.

The material is *strain-hardening* (resp. *softening*) if $\mathcal{R}$ is increasing (resp. *decreasing*) with α and *stress-hardening* (resp. *softening*) if $\mathcal{R}^*$ is increasing (resp. *decreasing*) with α (Marigo et al., 2016). The inspection of (25)-(27) reveals that this class of models enjoys the following properties:

- Strain-hardening if and only if $\gamma_\kappa > 1$ and $\gamma_\mu > 1$;
- Stress-softening for any $\gamma_\kappa > 0$ and $\gamma_\mu > 0$;

- Maximum allowable pressure and shear stress, coinciding with the elastic limit for purely volumetric and deviatoric states and given by:

$$p_{\text{peak}} := \bar{p}(0) = \sqrt{\frac{2\kappa_0 w_1}{\gamma_\kappa}} = \sqrt{\frac{2\kappa_0\, G_c}{\gamma_\kappa\, \pi\, \ell}}, \qquad \tau_{\text{peak}} := \bar{\tau}(0) = \sqrt{\frac{2\mu_0 w_1}{\gamma_\mu}} = \sqrt{\frac{2\mu_0\, G_c}{\gamma_\mu\, \pi\, \ell}}, \quad (28)$$

where we anticipated the relation $G_c = w_1 \pi \ell$ between the specific dissipation w_1, the fracture energy G_c, and the regularization length ℓ, that will be proved in the next section.

As detailed in (Pham et al., 2011a; Marigo et al., 2016), strain-hardening is equivalent to the convexity of the energy density $W(\boldsymbol{\varepsilon}, \alpha, 0)$ with respect to α at fixed $\boldsymbol{\varepsilon}$, whilst stress-hardening is equivalent to the convexity of W with respect to the full state $(\boldsymbol{\varepsilon}, \alpha)$. In the following we consider only models with strain-hardening and stress-softening. On one hand, stress-hardening model implies the uniqueness of the solution, and do not allow for localization of damage. On the other hand, strain-softening must be ruled out because poses mathematical and numerical difficulties.

2.5. Use of the `S-LS` model to control the peak stresses for hydrostatic and deviatoric states

The `S-LS` model (5) with independent softening parameters γ_μ and γ_κ is in principle very appealing. Indeed, one can control separately the nominal peak stress p_{peak} and τ_{peak} for purely isotropic and deviatoric stress states, by setting:

$$\gamma_\kappa = \frac{2G_c\kappa_0}{\pi\ell\, p_{\text{peak}}^2}, \quad \gamma_\mu = \frac{2G_c\mu_0}{\pi\ell\, \tau_{\text{peak}}^2}, \tag{29}$$

provided that the regularization length ℓ is chosen small enough to assure strain-hardening, *i.e.*:

$$\ell < \ell_{\max} := \min\left\{ \frac{2G_c\mu_0}{\pi\, \tau_{\text{peak}}^2}, \frac{2G_c\kappa_0}{\pi\, p_{\text{peak}}^2} \right\}. \tag{30}$$

With this choice, the ratio of the peak stresses for shear and hydrostatic states

$$\frac{\tau_{\text{peak}}}{p_{\text{peak}}} = \sqrt{\frac{\mu_0\gamma_\kappa}{\kappa_0\gamma_\mu}}$$

can be rendered independent of the ratio of the elastic moduli μ_0/κ_0 by controlling the ratio γ_κ/γ_μ. This additional flexibility is a improvement with respect to models with a single softening parameter. When the degradation function of the shear and bulk modulus coincide, *i.e.* $\gamma_\kappa = \gamma_\mu$, the strength ratio depends exclusively on the undamaged elastic moduli μ_0 and κ_0. As pointed out by Kumar et al. (2020), this appears as an important limitation of classical phase-field model in the modelling of crack nucleation. As a paradoxical example, for almost incompressible material $\kappa_0/\mu_0 \to \infty$, then $p_{\text{peak}} \to \infty$. This means that one cannot obtain nucleation of crack under isotropic loading states. This is not consistent with the experimental observations, as illustrated by Kumar and Lopez-Pamies (2021) for the case of the Poker-chip experiment on almost incompressible elastomers. More in general, independent tuning of the shear and isotropic strength is a necessary property for modelling crack nucleation under multi-axial stress states. Lorenzis and Maurini (2021); Vicentini et al. (2024) discussed how energy decompositions have an important influence on this aspect and can add additional flexibility on the shape to parametrically tuning the strength surface.

The independent control of the peak stresses for deviatoric and isotropic states induces to believe that this kind of issues is apparently solved in the `S-LS` model by setting the softening

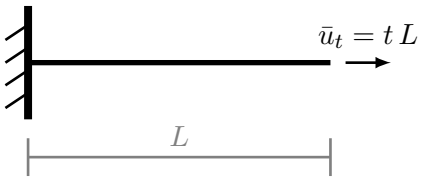

Figure 2: Uniaxial traction problem with imposed end-displacement $\bar{u}_t$.

parameters according to (29). However, the reasoning above assumes that the peak stress surface $\partial\mathcal{R}(\alpha_{\text{peak}})$ coincides with the strength surface at which cracks nucleate, as commonly accepted the literature (Kumar et al., 2020; Lorenzis and Maurini, 2021; Tanné et al., 2018). For uniaxial stress-states, this is justified by the stability and bifurcation analyses. Pham et al. (2011a); León Baldelli and Maurini (2021) show that, for *sufficiently large structures*, the peak stress corresponds to the critical loading at which solutions with homogeneous damage become state- and incrementally-unstable under imposed end-displacement. Extrapolating this result to multi-axial stress states leads to the identification of the peak stress surface $\partial\mathcal{R}(\alpha_{\text{peak}})$ with the strength surface (Kumar et al., 2020; Lorenzis and Maurini, 2021; Vicentini et al., 2024). The numerical nucleation tests of the next sections show that the actual response is more complex, and intriguing. They will show unexpected situations in which the assimilation of the peak stress with the strength, *i.e.* the critical load at which cracks nucleate, is abusive. The second-order stability analysis will reveal that the nucleation conditions under multi-axial stress states are more complex, and homogeneous states can be stable also in the softening regime, a point ignored in the literature on phase-field models of fracture.

In the rest of this work, we will discuss this issue in details. We will start with the one-dimensional case, which is amenable to a complete analytical treatment. We will extend the analysis to the multiaxial case in a second step.

3. Uniaxial traction test

We start considering the case of the uniaxial traction of a bar of length L with a monotonically increasing loading, see Figure 2. We assume in this section that the softening modulation parameter is the same for the spherical and deviatoric part of the energy $\gamma_\kappa = \gamma_\mu = \gamma$. For this specific model, full analytical expression of the homogeneous and localized solutions, including the stability limit of the homogeneous solution, are possible. On this basis, we will discuss the scale effects arising because of the competition between the structural leng-scale L, the cohesive length-scale ℓ_{ch} relate to the softening parameter γ, and the regularizing length-scale ℓ introduced through the gradient term in the damage. This will allow us to underpin the crack formation mechanisms and the non-trivial dependence of the numerical experiments on the model parameters.

3.1. Analytical solution of the 1d model

For the analytical solution, we use a one-dimensional bar model under an uniaxial stress hypothesis, as in Pham et al. (2011a). Denoting by $x \in (-L/2, L/2)$ the axial variable, the total energy per unit of width is:

$$\mathcal{E}(u,\alpha) := \int_{-L/2}^{L/2} \left(E_0 a(\alpha(x)) \frac{u'(x)^2}{2} + w_1 \left(w(\alpha(x)) + \ell^2\, \alpha'(x)^2 \right) \right) dx, \tag{31}$$

where,

$$a(\alpha) := \frac{1 - w(\alpha)}{1 + (\gamma - 1)\, w(\alpha)},$$

$u : x \in \Omega \equiv (-L/2, L/2) \to \mathbb{R}$ and $\alpha : x \in \Omega \to \mathbb{R}$ being the one-dimensional axial displacement and damage fields, $u'(x) = \frac{du(x)}{dx}$ and $\alpha'(x) = \frac{d\alpha(x)}{dx}$ their space derivatives. The sets for admissible displacement fields and damage fields are

$$\mathcal{C}_t \equiv \{u \in H^1(\Omega, \mathbb{R}),\, u(-L/2) = 0,\; u(L/2) = t\, L\}, \qquad \mathcal{D}_t(\alpha_t) \equiv \{\alpha \in H^1(\Omega, \mathbb{R}),\, \alpha_t \le \alpha < 1\}, \tag{32}$$

The 1d version of the equilibrium conditions (15) imposes the stress $\sigma_t = E_0\, a(\alpha_t)\, u_t'$ to be uniform throughout the bar. The damage criterion (16) writes as

$$\dot\alpha_t \ge 0,\; -\frac{\sigma_t^2}{2w_1 E_0} s'(\alpha_t) + w'(\alpha_t) - 2\ell^2 \alpha_t'' \ge 0,\; \left(-\frac{\sigma_t^2}{2w_1 E_0} s'(\alpha_t) + w'(\alpha_t) - 2\ell^2 \alpha_t''\right) \dot\alpha_t = 0. \tag{33}$$

where $s(\alpha) := 1/a(\alpha)$ is the 1d compliance function. In the absence of Dirichlet boundary conditions on the damage, the Neumann boundary conditions are $\alpha_t'(-L/2) \le 0$, $\alpha_t'(L/2) \ge 0$, with the complementary condition $\alpha_t'(-L/2) \cdot \dot\alpha_t(-L/2) = 0$, $\alpha_t'(L/2) \cdot \dot\alpha_t(L/2) = 0$ given by the energy balance. Two possible classes of solutions compete during the evolution problem:

(i) Solutions with homogeneous damage and strain;

(ii) Solutions with a damage localization, inside the domain or at the boundary.

We analyze below their properties.

3.1.1. Homogeneous solution

Solving the system of inequalities above for $\alpha'(x) = \alpha''(x) = 0$ gives the homogeneous solution which is also homogeneous in strain ($u'(x) = t$). Starting from an undamaged state $\alpha_0 = 0$, for

$$\sigma_t \le \sigma_{\text{peak}} := \sqrt{\frac{2w_1 E_0 w'(0)}{s'(0)}} = \sqrt{\frac{2w_1 E_0}{\gamma}} \quad \Leftrightarrow \quad t \le t_{\text{peak}} := \sqrt{\frac{2w_1}{\gamma E_0}} = \frac{\sigma_{\text{peak}}}{E_0} \tag{34}$$

the second inequality in (33) is strict and $\dot\alpha_t = 0$ because of the third complementary condition in (33). The solution is linear elastic in this range. For $t \ge t_{\text{peak}}$, the damage criterion must be verified as an equality. Solving this equation for α_t gives the damage evolution. Hence, the evolution of homogeneous damaged states under the monotonic increasing end-displacement tL is

$$\alpha_t^{\mathtt{H}} = \begin{cases} 0, & 0 \le t \le t_{\text{peak}}, \\ 1 - \sqrt{\dfrac{t_f - t}{t_f - t_{\text{peak}}}}, & t_{\text{peak}} \le t \le t_f, \\ 1, & t \ge t_f, \end{cases} \qquad \sigma_t^{\mathtt{H}} = \begin{cases} E_0\, t, & 0 \le t \le t_{\text{peak}}, \\ \sigma_{\text{peak}} \dfrac{t_f - t}{t_f - t_{\text{peak}}}, & t_{\text{peak}} \le t \le t_f, \\ 0, & t \ge t_f, \end{cases} \tag{35}$$

where $t_f = \gamma\, t_{\text{peak}} = \sqrt{\frac{2\gamma w_1}{E_0}}$.

3.1.2. Localised solution

Exploiting a change of variable $\alpha \leftrightarrow w$ (Alessi et al., 2014b), one finds the following family of solutions of (33) with damage localization centered in $x = \bar{x}$. These solutions are characterized by the homogeneous stress level $\bar{\sigma}$ at which the localization process initiates, starting from a homogeneous damage level $\bar{\alpha}$, and by the current stress σ, constant throughout the bar, with $0 \leq \sigma \leq \bar{\sigma} \leq \sigma_{\text{peak}}$, see Figure 3-left:

$$\alpha_{\text{loc}}(x;\sigma,\bar{\sigma},\bar{x}) = \begin{cases} 1 - \sqrt{\frac{\bar{\sigma}}{\sigma_{\text{peak}}}\left(1 - \left(1 - \frac{\sigma^2}{\bar{\sigma}^2}\right)\cos^2\left(\frac{x-\bar{x}}{\ell}\right)\right)}, & |x-\bar{x}| \leq \dfrac{\pi\ell}{2} \\ \bar{\alpha} = 1 - \sqrt{\frac{\bar{\sigma}}{\sigma_{\text{peak}}}}, & \text{otherwise} \end{cases}. \tag{36}$$

When the damage is not prescribed at the boundary as a Dirichlet condition, the localization can be centered at the bar ends with $\bar{x} = \pm L/2$ and only one-half of the profile should be considered. The energy dissipated for a localization initiated from the elastic solution ($\bar{\sigma} = \sigma_{\text{peak}}$, $\bar{\alpha} = 0$) and reaching the the stress level σ is

$$D_\sigma = 2m\int_0^{\bar{x}+\frac{\pi\ell}{2}} (w_1 w(\alpha(x)) + w_1\ell^2\alpha'(x)^2)dx = m w_1 \pi\ell\left(1 - \frac{\sigma}{\sigma_{\text{peak}}}\right), \tag{37}$$

where $m = 1$ for a full localization in the bulk and the $m = 1/2$ for half-localization at the boundary. The fracture toughness G_c is the energy D_0 dissipated in a fully developed crack in the bulk when reaching the stress level $\sigma = 0$. This gives the following relation between the toughness G_c, the specific material dissipation w_1 per unit volume, and the regularization length ℓ (we consider a crack in the a bulk, *i.e.* $m = 1$):

$$G_c = w_1 \pi\ell. \tag{38}$$

Integrating the strain field $u' = s(\alpha)\sigma/E_0$ across the localization band gives the relation between the displacement jump $[\![u]\!]$ at the ends of the localization, $\bar{x} \pm \pi\ell/2$, and the stress σ (see Figure 3-right) :

$$\sigma = \begin{cases} \frac{E_0[\![u]\!]}{m\pi\ell}, & 0 \leq [\![u]\!] \leq \frac{\sigma_{\text{peak}}}{E_0} m\pi\ell, \\ \dfrac{1 - \frac{\sigma_{\text{peak}}}{2mG_c}[\![u]\!]}{1 - \frac{\pi\ell\sigma_{\text{peak}}^2}{2E_0 G_c}}\sigma_{\text{peak}}, & \frac{\sigma_{\text{peak}}}{E_0} m\pi\ell \leq [\![u]\!] \leq \frac{2mG_c}{\sigma_{\text{peak}}}. \end{cases} \tag{39}$$

The expressions above are for a localization starting at $\bar{\sigma} = \sigma_{\text{peak}}$, $\bar{\alpha} = 0$. To emphasize the equivalence with cohesive-zone models, we replaced γ and w_1 with σ_{peak} and G_c, using (34) and (38), respectively. This point will be discussed in details later.

3.1.3. Global response

For a monotonically increasing loading starting from $t = 0$, the solution is purely elastic and unique for $t \leq t_{\text{peak}}$. For $t \geq t_{\text{peak}}$ the solution can be either with homogeneous or localized damage. Equation (35) gives the homogeneous solution. If the bar is long enough to host a damage localisation ($L > m\pi\ell$), solutions with damage localisation can start at any loading $\bar{t} \in [t_{\text{peak}}, t_f)$, branching from homogeneous solution at the damage level $\bar{\alpha} := \alpha_{\bar{t}}^{\mathtt{H}}$ and stress $\bar{\sigma} := \sigma_{\bar{t}}^{\mathtt{H}}$. The global force-displacement response of a bar is obtained by integrating $u' = s(\alpha)\sigma/E_0$ across the whole bar. For the one-parameter family of solutions obtained by

considering the bifurcation from the homogeneous solution happening at the critical loading $\bar{t} \in [t_{\text{peak}}, t_f)$, the global force-displacement response writes as :

$$\sigma = \begin{cases} E_0 t, & 0 \le t \le t_{\text{peak}} = \dfrac{\sigma_{\text{peak}}}{E_0}, \\ \sigma_t^{\mathtt{H}} = \dfrac{t_f - t}{t_f - t_{\text{peak}}}\, \sigma_{\text{peak}}, & t_{\text{peak}} \le t \le \bar{t}, \\ \sigma_{\bar{t}}^{\mathtt{H}}\, \dfrac{t_* - t}{t_* - \bar{t}}, & \bar{t} \le t \le t_* = m \dfrac{2G_c}{\sigma_{\text{peak}} L}, \\ 0, & t \ge t_*. \end{cases} \tag{40}$$

Figure 4 reports the global response of the bar graphically, showing several possible localised solutions (dashed line) branching from the homogeneous solution (solid line). For the specific model (5) at hand, not only the homogeneous response, but also the localized branches are straight lines, and the global response is piece-wise linear. The arrow indicates a possible loading path, with loading and unloading after a bifurcation from the homogeneous to a localized solution. The dark gray region represents the energy dissipated during the localization process, whilst the light gray region is the elastic energy that is released after the unloading. We discuss below how the relative ordering of the critical loads t_{peak}, t_f, and t_* characterizes the stability of the homogeneous states and the qualitative properties of the evolution.

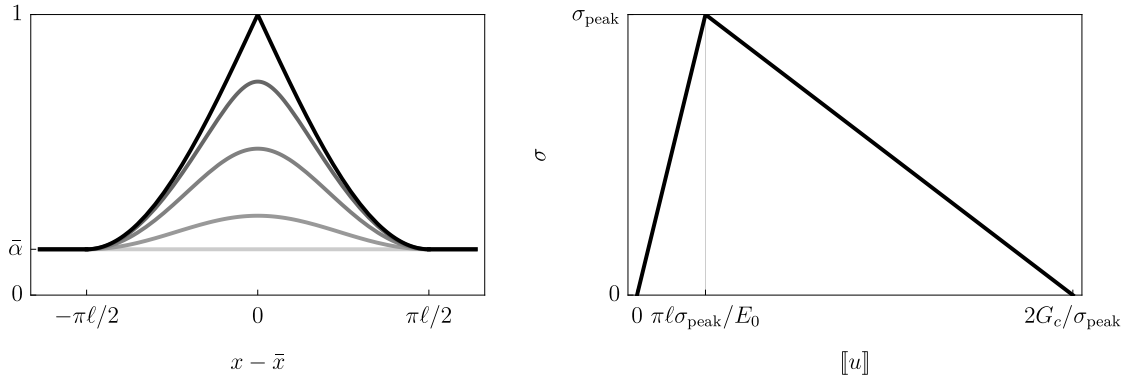

Figure 3: Localized solution for the 1d traction problem (analytical solution). Left: Damage field bifurcating from a solution with homogeneous damage $\bar{\alpha} := \alpha_{\bar{t}}^{\mathtt{H}} = 1 - \sqrt{\bar{\sigma}/\sigma_{\text{peak}}}$ for different stress levels from $\sigma = \bar{\sigma} \le \sigma_{\text{peak}}$ (light gray) to $\sigma = 0$ (black). Right: Relation between the stress σ and the displacement jump $[\![u]\!]$ across the localization band, representing the equivalent cohesive law, where the first phase with positive stiffness represents the homogeneous elastic response, whilst the softening phase corresponds to the development of the localization. Here we consider a full localization in the bulk, $m = 1$.

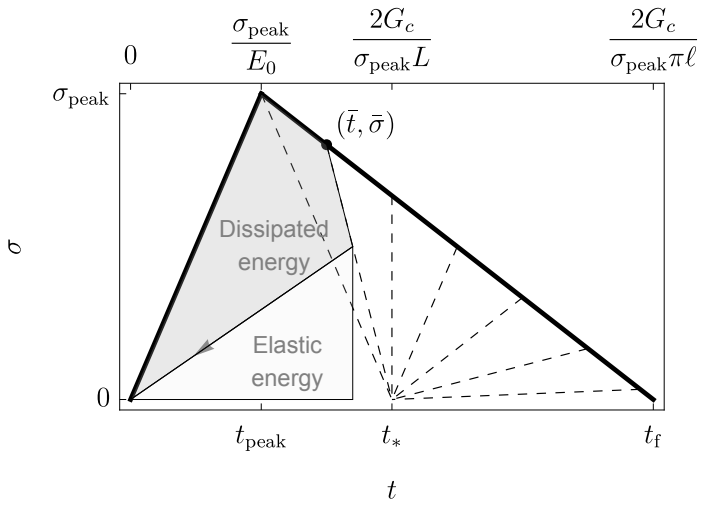

Figure 4: Global stress-displacement responses of a bar with homogeneous (solid line) and localised (dashed lines) solutions. Bifurcations from the homogeneous solution to a solution with localized damage is possible at any homogeneous damage $\bar{\alpha}$, as shown in Figure 3, corresponding to the end-displacement $\bar{t}$ and the stress $\bar{\sigma}$, see (40). Here we consider a full localization in the bulk, $m = 1$. The regions in gray illustrate the energetic interpretation of the areas under a generic loading path. The area under the curve is the sum of the energy dissipated during the localization process (dark-gray) and the elastic energy (light-gray) that can be released after the unloading (arrow).

3.2. Stability of homogeneous states

Crack nucleation can be understood as a bifurcation from the homogeneous solution to a solution with localized damage. As shown in Figure 4, for any loading $t \in [t_{\text{peak}}, t_f]$ the solution with homogeneous damage can coexist with infinitely many localized solution parameterized by the bifurcation loading $\bar{t}$. Studying the (un)stability of the homogeneous solution is therefore crucial to determine the crack nucleation threshold (Pham et al., 2011a). To this end, we resort to the definition of incremental- and state-stability of Section 2.2-2.3 and apply results of previous studies dedicated to the stability/bifurcation analysis (Pham et al., 2011a; León Baldelli and Maurini, 2021).

During the elastic stage, the first order terms of the expansion (13) are strictly positive, because the damage criterion is satisfied as a strict inequality. Hence, the elastic solution is incrementally- and state-stable. Damage, and cracks, cannot nucleate during this phase (Pham et al., 2011a).

Assessing the stability of the phase with homogeneous damage, requires to compute the second variation of the energy functional. The computations, reported in (Pham et al., 2011a; Marigo et al., 2016) for a generic model, lead to the following conditions for state-stability (SS) and incremental-stability (IS):

$$\begin{aligned} \text{SS}: \quad & \frac{L}{m\pi\ell} < \sqrt{\frac{32a(\alpha_t)^2 s'(\alpha_t)^4 \sigma_t^4/E_0^2}{w_1^2(s''(\alpha_t)\sigma_t^2/(E_0 w_1) - 2w''(\alpha_t))^3}} = \frac{\gamma\, t_{\text{peak}}}{t}, \\ \text{IS}: \quad & \frac{L}{m\pi\ell} < \sqrt{\frac{16}{s''(\alpha_t)\sigma_t^2/(E_0 w_1) - 2w''(\alpha_t)}} = 1, \end{aligned} \tag{41}$$

where $m = 1/2$ if one allows for damage localization at the boundary or $m = 1$ if one imposes $\alpha(\pm L/2) = 0$ and allows for damage localization in the bulk only. As expected, IS implies SS. The inequalities with the opposite signs are sufficient conditions for state- and incremental-instability, respectively.

Figure 5 summarizes the analytical results for the 1d-traction problem, reporting the stability diagram of the homogeneous solution as a function of the bar length and the loading (left) and the global force-displacement response (right) for the homogeneous (solid lines) and localized solutions (dashed lines). For the present model, the homogeneous and the localized solution lead to final failure for the finite loads t_f and t^*, respectively. The figure discloses several interesting scale-effects for a bar of finite length L, with three qualitatively different regimes, depending of the relative ordering of t_{peak}, t_f and t_*:

- For very short bars with $L < m\pi\ell$ (left-bottom), $t_* > t_f$ and the solution with homogeneous damage is incrementally-stable and state-stable for any loading. In this regime, solutions with localized damage does not exist, because the bar is too short to host a localization zone of size $m\pi\ell$.
- For bars of intermediate lengths, $m\pi\ell < L < \gamma\, m\pi\ell = m\frac{2G_cE_0}{\sigma^2_{\text{peak}}} = m\,\ell_{\text{ch}}$ (left-center), $t_{\text{peak}} < t_* < t_f$ and bifurcations from the homogeneous solution with damage localization are possible after the elastic limit. The homogeneous solution is incrementally-unstable, being state-stable for $t < t_* = 2m\frac{G_c}{\sigma_{\text{peak}}L}$ and state-unstable for larger loadings.
- For long bars with $L > m\frac{2G_cE_0}{\sigma^2_{\text{peak}}} = m\,\ell_{\text{ch}}$ (left-top), after the elastic limit the homogeneous solution is state-unstable (hence, incrementally-unstable). The localised solutions always exhibit a snap-back in the global strain-stress response.

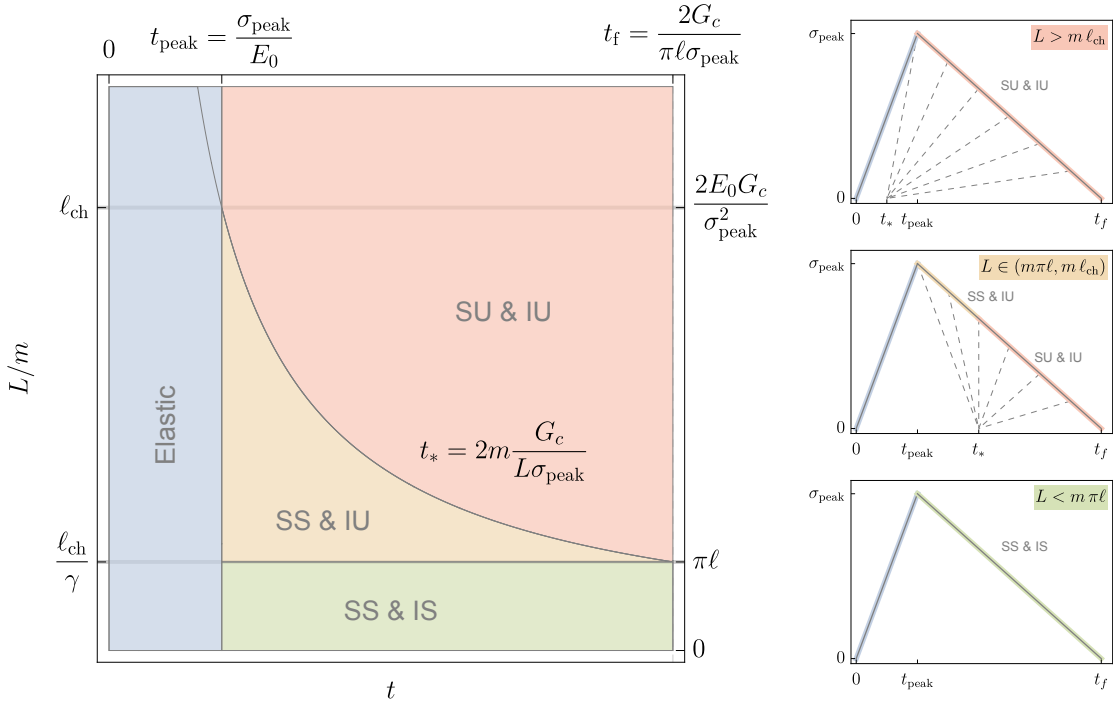

Figure 5: Analytical solution for the 1d traction problem. Left: stability diagram of the homogeneous solution with purely elastic states in blue, state-stable (SS) states and incrementally-stable (IS) states in green, state-stable (SS) states and incrementally-unstable (IU) states in orange, state-unstable (SU) and incrementally-unstable (IU) states in red. Right: global force-displacement diagrams in the three qualitatively different regimes representing the stress σ as a function of the imposed average strain t. The solid lines are for solution with homogeneous damage and strain (35), whilst dashed lines are for the localised responses bifurcating from the homogeneous solution for different initial damage levels $\bar{\alpha}$, see (40).

Free parameters	G_c	w_1	γ	ℓ	σ_{peak}	t_{peak}	t_*	t_f	ℓ_{ch}
E_0, G_c, γ, ℓ	G_c	$\frac{G_c}{\pi\ell}$	γ	ℓ	$\sqrt{\frac{2G_cE_0}{\pi\ell\gamma}}$	$\sqrt{\frac{2G_c}{\pi\ell\gamma E_0}}$	$\frac{1}{L}\sqrt{\frac{2\pi\ell\gamma G_c}{E_0}}$	$\sqrt{\frac{2G_c\gamma}{\pi\ell E_0}}$	$\pi\gamma\ell$
$E_0, G_c, \gamma, \sigma_{\text{peak}}$	G_c	$\frac{G_c}{\pi\ell}$	γ	$\frac{2G_cE_0}{\pi\gamma\sigma_{\text{peak}}^2}$	σ_{peak}	$\frac{\sigma_{\text{peak}}}{E_0}$	$\frac{2G_c}{\sigma_{\text{peak}}L}$	$\gamma\frac{\sigma_{\text{peak}}}{E_0}$	$\frac{2G_cE_0}{\sigma_{\text{peak}}^2}$
$E_0, G_c, \sigma_{\text{peak}}, \ell$	G_c	$\frac{G_c}{\pi\ell}$	$\frac{2G_cE_0}{\pi\ell\sigma_{\text{peak}}^2}$	ℓ	σ_{peak}	$\frac{\sigma_{\text{peak}}}{E_0}$	$\frac{2G_c}{\sigma_{\text{peak}}L}$	$\frac{2G_c}{\pi\ell\sigma_{\text{peak}}}$	$\frac{2G_cE_0}{\sigma_{\text{peak}}^2}$
E_0, w_1, γ, ℓ	$\pi w_1\ell$	w_1	γ	ℓ	$\sqrt{\frac{2w_1E_0}{\gamma}}$	$\sqrt{\frac{2w_1}{\gamma E_0}}$	$\frac{\pi\ell}{L}\sqrt{\frac{2\gamma w_1}{E_0}}$	$\sqrt{\frac{2w_1\gamma}{E_0}}$	$\pi\gamma\ell$

Table 1: Expression of the relevant model quantities for different free-parameter sets ($m = 1$, *i.e.* for cracks corresponding to localizations in the bulk).

Note that the state-stability threshold for the homogeneous solution corresponds to the snap-back threshold for the global $\sigma-t$ response of the localized solution, as already highlighted in Pham and Marigo (2013b).

3.3. Material parameters, length-scales, and dimensionless parameters

The expressions (5) for the constitutive functions adopt the independent material parameters w_1, ℓ, γ. The solution of the bar traction problem shows how the peak load σ_{peak} and the toughness G_c are related to these parameters. Using these relations, one can use these derived quantities of primary applicative interest as independent parameters. First, focusing on fracture phenomena governed by damage localization in crack-like bands, one can replace the dissipation per unit of volume w_1 by the dissipation per unit surface G_c as dissipation parameter using (38). Moreover, instead of regarding the softening parameter γ as a free parameter, one can set it to control the peak stress, using (34):

$$\gamma = \frac{2E_0w_1}{\sigma_{\text{peak}}^2} = \frac{2G_cE_0}{\pi\ell\sigma_{\text{peak}}^2} = \frac{\ell_{\text{ch}}}{\pi\ell}. \tag{42}$$

Table 1 collects the expressions of the relevant model quantities for different parametrizations of the constitutive model. We classify four different relevant parametrizations, according to the sets of free parameters:

- (E_0, G_c, γ, ℓ) corresponds to the classical presentation of phase-field models of brittle fracture, where the softening parameter γ (or an analogous quantity) is a free parameter independent of the material length-scale, and the peak stress σ_{peak} is a derived quantity, depending on ℓ. In agreement with gamma-convergence results, for $\ell \to 0$, one obtains a finite Griffith-like brittle fracture model, with a finite fracture toughness G_c, but an infinite strength $\sigma_{\text{peak}} \to \infty$ and a vanishing cohesive length-scale $\ell_{\text{ch}} \to 0$.

- $(E_0, G_c, \gamma, \sigma_{\text{peak}})$ corresponds to the parametrization used in Amor et al. (2009) and Tanné et al. (2018) to obtain crack nucleation with finite and controlled peak stress σ_{peak} in uniaxial traction, while keeping a finite and controlled fracture toughness G_c. With this choice the regularization length-scale ℓ, becomes a dependent parameter, that should be set according to Table 1. The model can be interpreted as a quasi-brittle damage model, with well-defined specific dissipation w_1, toughness G_c and cohesive length-scale ℓ_{ch}.

- $(E_0, G_c, \sigma_{\text{peak}}, \ell)$ exploits the softening modulation γ to independently control the peak stress σ_{peak}, the toughness G_c, and the regularization length-scale ℓ (Lorentz et al.,

2011). Note however, that the energy dissipation per unit volume w_1 diverges as ℓ^{-1} for $\ell \to 0$: homogeneous damage states are not allowed in this limit.

- (E_0, w_1, γ, ℓ) corresponds to a regularized damage model, where, for vanishing regularization length ℓ, keeps fixed the properties of the homogeneous damage response (specific dissipation, softening modulus and peak stress) whilst the toughness becomes a ℓ-dependent quantity, with $G_c \to 0$ for $\ell \to 0$.

A dimensional analysis reveals that two of the four parameters can be eliminated by a simple variable rescaling. The material parameters above introduce two length-scales: the cohesive length-scale ℓ_{ch} and the regularization (or localization) length-scale ℓ. These two length-scales compete with the structural length-scale $L = |\Omega|$. We select ℓ_{ch} as reference length, and defines the following dimensionless parameters :

$$\lambda_{\text{str}} := \frac{L}{\ell_{\text{ch}}} = \frac{L\sigma_{\text{peak}}^2}{2G_c E_0}, \quad \lambda_{\text{reg}} := \frac{\ell}{\ell_{\text{ch}}} = \frac{1}{\pi\gamma}, \tag{43}$$

representing the dimensionless structural length and the dimensionless regularization length-scale, respectively. The model responses depends on this two dimensionless parameters only.

3.4. Numerical simulations of the uniaxial traction test

We perform different numerical experiments on the bar under uniaxial traction shown in Figure 6.

We solve here a problem on two-dimensional geometry under plane-stress conditions. We consider a rectangular domain of length $L = 1$ and height $H = 0.1$, setting the Poisson ratio to $\nu = 0.3$. We apply free-sliding conditions at the left- and right-end, setting $u_x(0, y) = 0$ at the left-end and prescribing the traction loading $u_x(x = L, y) = t\,L$ at the right-end. Rigid-body modes are prevented by fixing the displacement in the y-direction at a single node on the left-end. The top and bottom boundaries are free. To rule out damage localization at the boundaries, we impose the Dirichlet boundary condition $\alpha = 0$ on both sides of the bar. We consider evolutions under monotonically increasing loading $t \geq 0$, starting with an intact material ($\alpha = 0$) at $t = 0$ as the initial condition. The problem is discretized using standard triangular finite elements with an unstructured mesh, where the average element size is $h = \ell/5$. Figure 6 shows a typical mesh and the localized damage field corresponding to a fully developed crack. Without loss of generality (see the previous section on dimensional analysis), we set $\sigma_{\text{peak}} = 1$.

At each time step t, we look for solutions of the nonlinear variational inequalities (14) by using the classical alternate minimization scheme and nonlinear bound-constrained solvers provided by `PETSc` (Balay et al., 2023). Hence, we check the (incremental) stability (19) of the solution found via the second-order stability check algorithm presented in (León Baldelli and Maurini, 2021). This algorithm tests the sign of the eigenvalues of a reduced hessian matrix eliminating the degrees-of-freedom where the irreversibility constraints are active. Both these algorithms are implemented in `FEniCSx` (Dokken et al., 2023). The reader can refer to (León Baldelli and Maurini, 2021) for further details.

First, to illustrate the three different possible qualitative behaviors from the stability diagram of Figure 5, we report in Figure 7 the numerical solutions obtained for three sets of parameters, that are classified as relatively long bars ($\pi\ell < \ell_{\text{ch}} < L = 1$, Figure 7a), intermediate bars ($\pi\ell < L = 1 < \ell_{\text{ch}}$, Figure 7b), and short bars ($1 = L < \pi\ell < \ell_{\text{ch}}$, Figure 7c). For each set of parameters, we present the global force-displacement response (left), the evolution of elastic and dissipated energy with loading (center), and the damage field along the

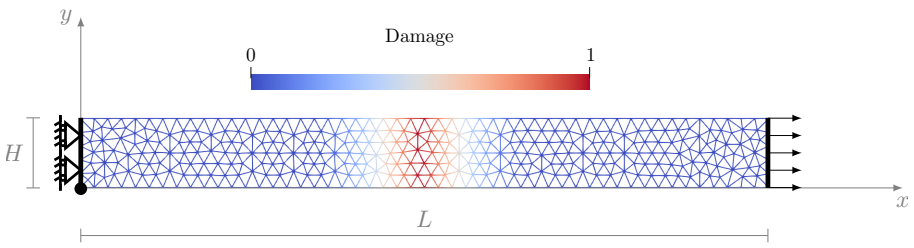

Figure 6: Geometry, boundary conditions, mesh of the bar and typical localized damage field for the 2d numerical simulations.

mid-line of the bar at different time instants (right). The parameter values and corresponding dimensionless lengths are displayed at the top of each figure. In the force-displacement response, we include the results of the second-order stability analysis of the solution found: green markers indicate incrementally-stable (IS) states, while red markers in green indicate an incrementally-unstable (IU) solution. For comparison, the analytical solution is shown as solid lines (localized solution) and dashed lines (homogeneous solution) in the force-displacement response. All the tests in Figure 7 for $E_0/\sigma_{\text{peak}} = 1$.

We observe the following behaviour:

- For sufficiently *long* bars (Figure 7a), at the peak load $t = t_{\text{peak}}$ the homogeneous solution is unstable and we observe the sudden transition from an elastic solution to a fully developed localized solution with $\sup_\Omega(\alpha) = 1$ and $\sigma = 0$. This condition corresponds to the presence of a snap-back in all the possible localized solutions ($t_* < t_{\text{peak}}$). We characterized this behavior as *brittle*.

- For bars with *intermediate* length (Figure 7b), we observe an incrementally-stable localized solution that evolves without abrupt transitions. Once the peak stress is reached, even if the damage field localizes with $\sup_\Omega(\alpha)$ increasing smoothly over time, without snap-backs ($t_* > t_{\text{peak}}$). This is consistent with the analytical results, for which the homogeneous solution is state-stable but incrementally-unstable (bifurcations are possible). In addition, the numerical stability analysis reveals that the localized solutions are incrementally-stable (all the points in the Figure 7b-left are green), a result that was not accessible from the analytical calculations. We characterized this behavior as *cohesive*.

- For very *short* bars (Figure 7c), the numerical results show the smooth development of a non-homogeneous diffuse damage field $t_* > t_{\text{f}} > t_{\text{peak}}$, which is stable. The theoretical stability analysis predicts that the homogeneous solution is state-stable and incrementally-stable in this case. However, the homogeneous solution is forbidden by the boundary conditions on the damage field setting $\alpha = 0$ at the left- and right-end. The numerical solvers produce a non-trivial solution with a diffuse damage field, which was not considered in the analytical study. Comparing the numerical results with the continuous gray line in the plot on the left panel, we can see that this solution has a force-displacement response that closely matches the analytical prediction for a bar with an effective length greater than L.

3.5. Energetic interpretation of the transition from brittle to cohesive behavior

The transition from the brittle to the cohesive behavior has a relevant and immediate energetic interpretation that can be deduced from the energetic interpretation of the areas

$G_c/(\sigma_{\text{peak}}L) = 0.25$, $E_0/\sigma_{\text{peak}} = 1.00$, $\ell/L = 0.100$ ($\lambda_{\text{str}} = 2.000$, $\lambda_{\text{reg}} = 0.20$)

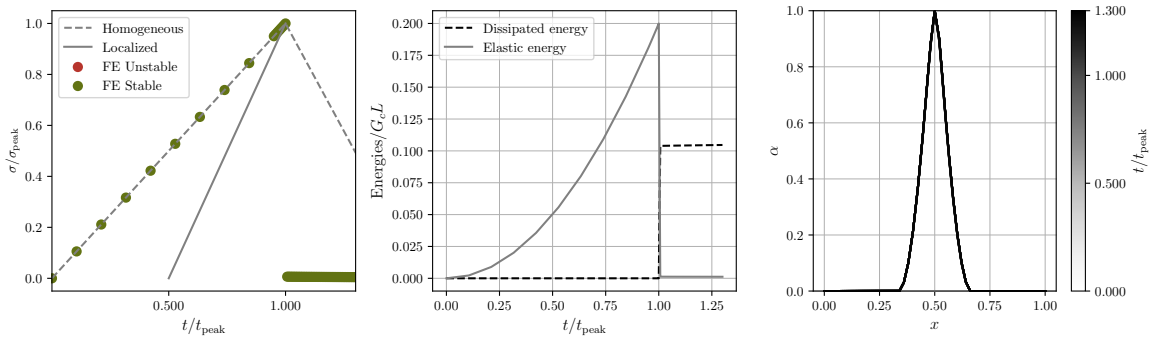

(a) Long bar with $L > \ell_{\text{ch}} > \pi\ell$, see Figure 5 (case right-top in red).

$G_c/(\sigma_{\text{peak}}L) = 1.00$, $E_0/\sigma_{\text{peak}} = 1.00$, $\ell/L = 0.100$ ($\lambda_{\text{str}} = 0.500$, $\lambda_{\text{reg}} = 0.05$)

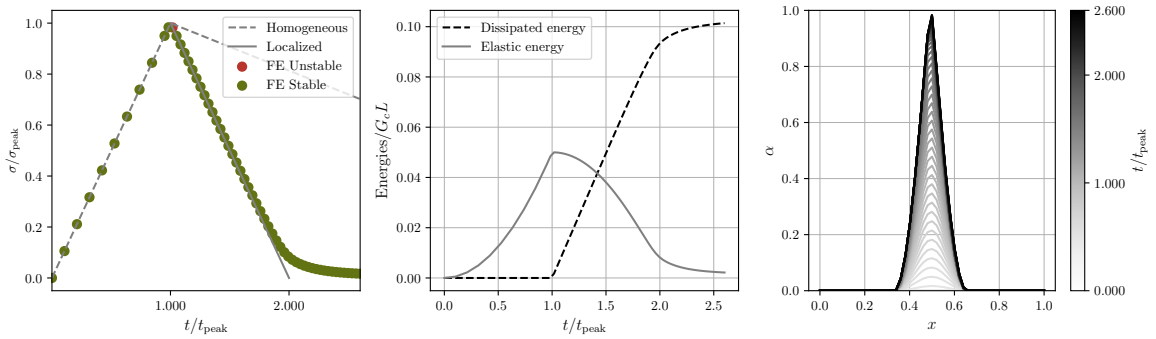

(b) Intermidiate-length bar with $L \in (\pi\ell, \ell_{\text{ch}})$, see Figure 5 (case right-center in orange).

$G_c/(\sigma_{\text{peak}}L) = 1.00$, $E_0/\sigma_{\text{peak}} = 1.00$, $\ell/L = 0.500$ ($\lambda_{\text{str}} = 0.500$, $\lambda_{\text{reg}} = 0.250$)

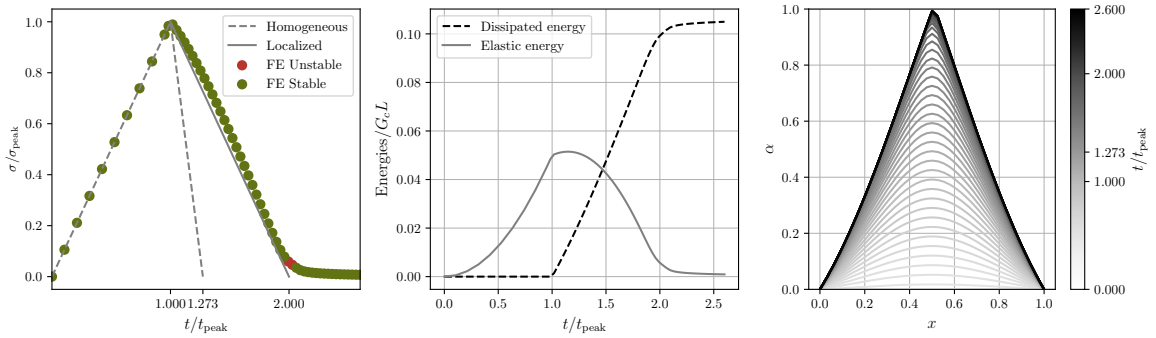

(c) Short bar with $L < \pi\ell$, see Figure 5 (case right-center in orange).

Figure 7: Numerical solution for the 1d traction problem different values of the parameters $G_c/(\sigma_{\text{peak}}L)$ ℓ/L corresponding to the three cases in Figure 5. Left: global force-displacement diagrams representing the stress $\sigma/\sigma_{\text{peak}}$ as a function of the imposed average strain t/t_{peak}. The green (incrementally stable) and red (incrementally unstable) dots are the result of the numerical finite element simulations on the 2d geometry, the gray solid lines correspond to the analytical localized responses bifurcating from the homogeneous solution in $\alpha = 0$, see (40), the gray dashed dotted lines to the solution with homogeneous damage and strain (35). Center: elastic and dissipated energies. Right: evolution of damage fields α along the mid-line of the bar for increasing values of the loading t.

under the force displacement diagram of Figure 4 and the energy diagram in the center column of Figure 7:

- If at the peak loading t_{peak} the elastic energy $L\sigma_{\text{peak}}^2/2E_0$ is larger than the energy required to create a fully developed crack, G_c, the solution exhibits a brutal transition from the elastic to the cracked state, with a snap-back in the global force-displacement response. This is the case of Figure 7a for which $\lambda_{\text{str}} = L/\ell_{\text{ch}} > 1$.
- If at the peak loading $L\sigma_{\text{peak}}^2/2E_0 < G_c$ ($\lambda_{\text{str}} = L/\ell_{\text{ch}} < 1$), there is not enough energy to create instantaneously a fully developed crack. The crack can develop only at the expense of the external working, leading to a smooth transition from the elastic to the cracked state controlled by the end-displacement. This is the case of Figure 7b.

Interestingly, the energetic condition above on $\lambda_{\text{str}} = L/\ell_{\text{ch}}$ coincides with the critical conditions for the stability of the homogeneous solution at the peak loading and the presence of a snap-back in the localized response.

3.6. The case of almost inextensible bars

Kumar et al. (2020) raised the interesting question of the crack nucleation conditions and strength in the case of almost incompressible materials. The equivalent condition for the 1d traction problem is that the bar is almost inextensible, *i.e.* $E_0/\sigma_{\text{peak}} \to \infty$. Figure 8 reports the response of a bar with $E_0/\sigma_{\text{peak}} = 50$, with $G_c/\sigma_{\text{peak}}L = 0.25$ and $\ell/L = 0.1$. The present model allows us to set the peak stress σ_{peak} independently of the Young modulus E_0, and the regularization length ℓ independently of the peak stress σ_{peak}, provided that it is sufficiently small compared to the bar length L. However, the crack cannot develops instantaneously at the peak load, as the energy required to create a fully developed crack is larger than the elastic energy stored in the bar. In the inextensible limit, the stored elastic energy at the peak load is vanishing and $\ell_{\text{ch}} \to \infty$. We are in the case of the bar of intermediate length with a cohesive response of Figure 7b, and the crack development is stable. The end-displacement controls the crack development process. In absence of sufficient elastic energy to be released, the loading device progressively provides the energy required to create the crack.

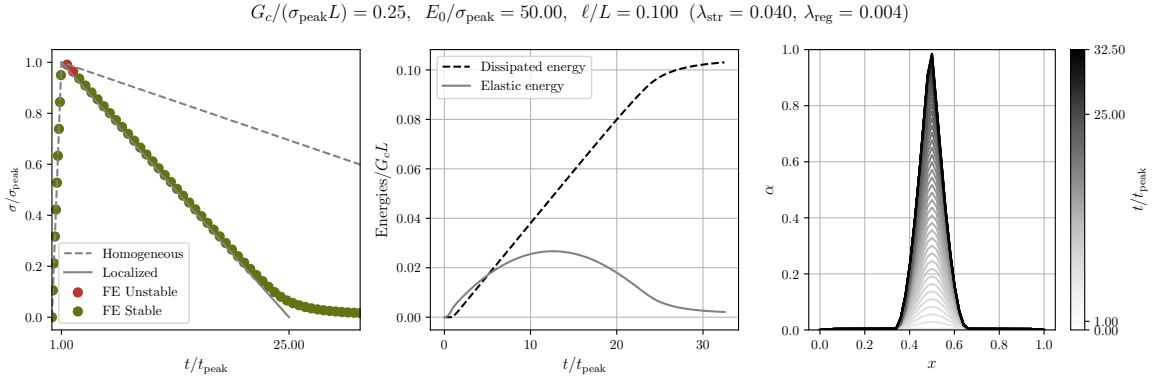

Figure 8: The response of an almost inextensible bar. In this case $L < \ell_{\text{ch}} \to \infty$ and the crack development is stable, as in Figure 7b. The evolution is smooth and controlled by the end-displacement, which provides the energy dissipated in the crack development process.

Our stability analysis and energetic arguments suggest that a brittle behavior, with a sudden unstable nucleation of a crack at a fixed end-displacement, is impossible for infinitely

stiff materials. Indeed, a brittle behavior requires a sufficient amount of elastic energy to be released in the crack creation process and compensate the dissipated energy G_c. This is consistent with the classical theory of fracture of Griffith (1921) and Irwin (1958). To force a brittle behavior also in the case of limited or absent elastic energy, Kumar et al. (2020) adds an "external" driving force, independent of the elastic energy release, in the damage criterion. The thermodynamic consistency of similar non-energetic approaches is questionable, as the origin of the energy provided by the driving force remains to be specified.

3.7. Issues for $\ell \ll \ell_{\text{ch}}$ ($\gamma \to \infty$)

The analytical results indicate that, for sufficiently long bars ($L > \ell_{\text{ch}}$), the model (5) with the softening modulation parameters γ set according to (42) gives a peak stress and a toughness independent of the regularization length ℓ. Yet, the volumetric dissipation parameters w_1 become very large for $\ell \to 0$. We observe that in these situations the classical alternate minimization solver can stagnate in unstable solutions with diffuse damage fields, instead of finding the localized solutions, as shown in Figure 9. The use of a second-order stability analysis is crucial to identify the (un)stable solutions. More sophisticated path-selection algorithms (León Baldelli and Maurini, 2021) or coupled solvers are required to retrieve the lower energy branch.

The use of a regularization length ℓ that is much smaller than the Irwin length ℓ_{ch} is rarely feasible from the computational point of view, because it requires a very fine mesh ($\ell \approx h/4$) to correctly discretize the localized solutions. Vice-versa, setting $\ell > \ell_{\text{ch}}/\pi$ ($\gamma < 1$) poses main issues, as the model becomes strain-softening. The homogeneous solution at imposed strain is not unique in this case, and numerical and theoretical problems arise.

In most situations, the more convenient setting is to use a regularization length ℓ that is of the same order of magnitude as the Irwin length ℓ_{ch}. In this case, the model behaves similarly as the classical $\texttt{AT}_1$ and $\texttt{AT}_2$ phase-field models of brittle fracture Tanné et al. (2018), with a peak stress that are related to the regularization length ℓ. Whenever separate experimental data on the energy dissipated in localized damage solution, G_c, and diffuse damage solutions are available, w_1, ℓ should ideally be adjusted according to the relation (38). Indeed, while the properties of localized solutions are independent of ℓ, the properties (and the stability) of diffuse damage solutions are not, as shown in Figure 5.

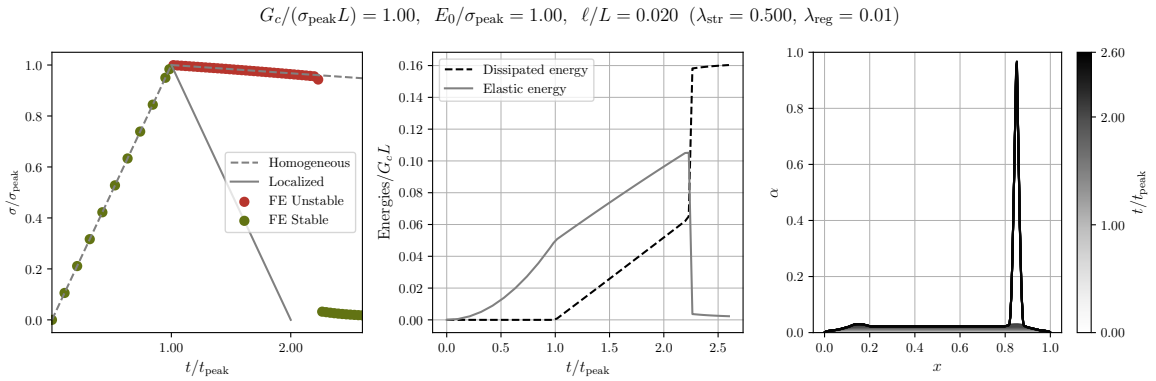

Figure 9: Numerical solutions of the bar problem for $\ell \ll \ell_{\text{ch}}$. The numerical solvers stagnate in unstable solutions with diffuse damage fields. The use of a second-order stability analysis is crucial to identify the (un)stable solutions (in red).

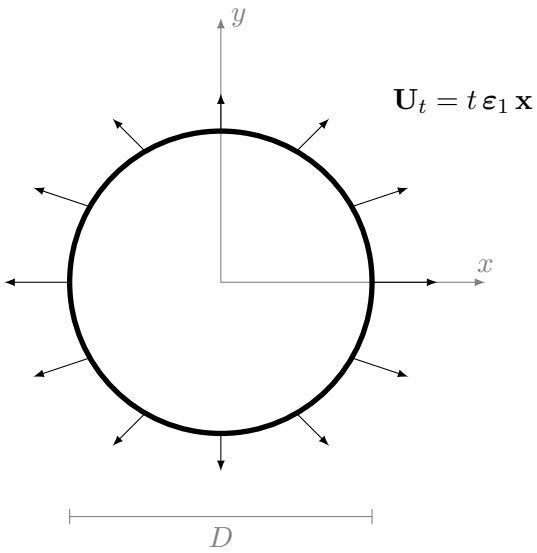

Figure 10: Geometry and loading for the bi-axially loaded disk.

4. Model behavior under multi-axial stress states

This section discusses the behavior of the `S-LS` model (5) under multi-axial stress states. To this end, we consider a disk Ω in 2d with a Dirichlet boundary condition

$$\mathbf{U}_t(\mathbf{x}) = t\,\boldsymbol{\varepsilon}_1\,\mathbf{x} \quad \text{on} \quad \partial\Omega, \quad \text{with} \quad \boldsymbol{\varepsilon}_1 = \frac{\cos\theta + \sin\theta}{2}\,(\boldsymbol{e}_x \otimes \boldsymbol{e}_x) + \frac{\cos\theta - \sin\theta}{2}\,(\boldsymbol{e}_y \otimes \boldsymbol{e}_y), \tag{44}$$

and the initial condition $\alpha_0 = 0$, see Figure 10. The loading is monotonically increasing with the scalar loading parameter t. The angle θ determines the multiaxial loading mode. The magnitude the spherical and deviatoric parts of the homogeneous strain $\boldsymbol{\varepsilon}_t = t\,\boldsymbol{\varepsilon}_1$ compatible with the boundary condition are

$$\varepsilon_t^{\text{iso}} := \operatorname{tr}(\boldsymbol{\varepsilon}_t) = t\cos(\theta), \quad \varepsilon_t^{\text{dev}} := \sqrt{2}\,|\boldsymbol{\varepsilon}_t^{\text{dev}}| = t\sin(\theta). \tag{45}$$

We parametrize the model by the elastic moduli (κ_0, μ_0) and the peak stress (p_{peak},τ_{peak}) for the isotropic and deviatoric modes, the fracture toughness G_c, and the regularization length ℓ. Hence, we rewrite the energy density (3) in the following form :

$$W(\boldsymbol{\varepsilon}, \alpha, \nabla\alpha) = \frac{\kappa_0}{2}\operatorname{tr}^-(\boldsymbol{\varepsilon})^2 + \frac{\kappa(\alpha)}{2}\operatorname{tr}^+(\boldsymbol{\varepsilon})^2 + \mu(\alpha)\,|\boldsymbol{\varepsilon}^{\text{dev}}|^2 + \frac{G_c}{\pi}\left(\frac{1-(1-\alpha)^2}{\ell} + \ell|\nabla\alpha|^2\right), \tag{46}$$

with

$$\kappa(\alpha) := \frac{(1-\alpha)^2}{1 + \left(\frac{2G_c\kappa_0}{\pi\ell\,p_{\text{peak}}^2} - 1\right)(1-(1-\alpha)^2)}\kappa_0, \quad \mu(\alpha) := \frac{(1-\alpha)^2}{1 + \left(\frac{2G_c\mu_0}{\pi\ell\,\tau_{\text{peak}}^2} - 1\right)(1-(1-\alpha)^2)}\mu_0, \tag{47}$$

where the softening parameters γ_κ and γ_μ are set according to the equations (29) and $w_1 = \frac{G_c}{\pi\ell}$.

We assume that the regularization length-scale ℓ is set to a sufficiently small value so that the strain-hardening condition is satisfied, see (30).

4.1. Homogeneous solutions

Homogeneous states automatically satisfy the equilibrium equation. A trivial solution for the displacement field is $\mathbf{u}_t(\mathbf{x}) = t\,\boldsymbol{\varepsilon}_1\,\mathbf{x}$, for all $\mathbf{x} \in \Omega$, with the homogeneous strain $\boldsymbol{\varepsilon}_t = t\,\boldsymbol{\varepsilon}_1$. The evolution of damage (and the stress) can be found by solving the system of inequalities:

$$\dot{\alpha}_t \geq 0, \quad t^2 \left(\frac{\mathrm{tr}^+ (\boldsymbol{\varepsilon}_1)^2}{\bar{\varepsilon}_\kappa(\alpha)^2} + \frac{2|\boldsymbol{\varepsilon}_1^{\mathrm{dev}}|^2}{\bar{\varepsilon}_\mu(\alpha)^2} \right) - 1 \geq 0, \quad \dot{\alpha}_t \cdot \left(t^2 \left(\frac{\mathrm{tr}^+ (\boldsymbol{\varepsilon}_1)^2}{\bar{\varepsilon}_\kappa(\alpha)^2} + \frac{2|\boldsymbol{\varepsilon}_1^{\mathrm{dev}}|^2}{\bar{\varepsilon}_\mu(\alpha)^2} \right) - 1 \right) = 0. \tag{48}$$

The solution is purely elastic until the strain is inside the initial elastic domain $\mathcal{R}(0)$. When it reaches the boundary, the damage starts increasing monotonically, until attaining the fully damaged state $\alpha = 1$. During the damage process the strain domain $\mathcal{R}$ expands (strain-hardening), whilst the stress domain $\mathcal{R}^*$ shrinks (stress-softening).

For purely isotropic loading ($\theta = 0$), with $\varepsilon_t^{\mathrm{iso}} = t$, $\varepsilon_t^{\mathrm{dev}} = 0$, the response is purely elastic for $t \leq \bar{\varepsilon}_\kappa(0) = p_{\mathrm{peak}}/\kappa_0$. For $t \geq \bar{\varepsilon}_\kappa(1) = \gamma_k \bar{\varepsilon}_\kappa(0) = \frac{2G_c}{p_{\mathrm{peak}}\pi\ell}$ the full damage level is attained and the stress is zero. For intermediate values, the damage is found by solving the damage criterion as an equality. This gives the following strain-stress response, see Figure 11-left:

$$\boldsymbol{\sigma}_t = p_t\,\boldsymbol{I}, \qquad p_t = \begin{cases} \kappa_0\,t, & t \leq \frac{p_{\mathrm{peak}}}{\kappa_0}, \\ p_{\mathrm{peak}} \dfrac{t - \frac{2G_c}{p_{\mathrm{peak}}\pi\ell}}{\frac{p_{\mathrm{peak}}}{\kappa_0} - \frac{2G_c}{p_{\mathrm{peak}}\pi\ell}}, & t \in \left[\frac{p_{\mathrm{peak}}}{\kappa_0}, \frac{2G_c}{p_{\mathrm{peak}}\pi\ell} \right], \\ 0, & t \geq \frac{2G_c}{p_{\mathrm{peak}}\pi\ell}. \end{cases} \tag{49}$$

The purely deviatoric loading mode ($\theta = \pi/2$), with $\varepsilon_t^{\mathrm{iso}} = 0$, $\varepsilon_t^{\mathrm{dev}} = t$ leads to an analogue response, where the deviatoric constants replace the spherical counterparts:

$$\boldsymbol{\sigma}_t = \frac{\boldsymbol{\varepsilon}_1^{\mathrm{dev}}}{|\boldsymbol{\varepsilon}_1^{\mathrm{dev}}|}\sqrt{2}\,\tau_t, \qquad \tau_t = \begin{cases} \mu_0\,t & t \leq \frac{\tau_{\mathrm{peak}}}{\mu_0}, \\ \tau_{\mathrm{peak}} \dfrac{t - \frac{2G_c}{\tau_{\mathrm{peak}}\pi\ell}}{\frac{\tau_{\mathrm{peak}}}{\kappa_0} - \frac{2G_c}{\tau_{\mathrm{peak}}\pi\ell}}, & t \in \left[\frac{\tau_{\mathrm{peak}}}{\kappa_0}, \frac{2G_c}{\tau_{\mathrm{peak}}\pi\ell} \right], \\ 0, & t \geq \frac{2G_c}{\tau_{\mathrm{peak}}\pi\ell}. \end{cases} \tag{50}$$

Figure 11 reports the homogeneous stress-strain response under monotonically increasing loading for purely volumetric (left) and purely deviatoric (right) loading modes. The plot is for $\kappa_0 = 1$, $\mu_0 = 1/3$ and $\tau_{\mathrm{peak}} = 0.5$, $p_{\mathrm{peak}} = 1.0$. The light-gray area under the stress curve is the dissipated energy in a homogeneous damage process $w_1 = \frac{G_c}{\pi\ell}$ and must coincide for the two loading modes. In this example, we set $G_c = 0.1$ and $\ell = 0.55\,\ell_{\max}$, $\ell_{\max}$ being the maximal value of the regularizing length-scale to assure the strain-hardening condition, see (30).

4.2. Multi-axial nucleation test

To investigate the crack nucleation threshold under multi-axial stress states, we perform different numerical experiments on the bi-axially loaded disk. At $t = 0$, the material is intact, *i.e.* $\alpha = 0$ everywhere. Maintaining θ fixed, we increment the value of t up to the point when a crack appears. We identify this critical load as the nucleation threshold of the material under the given loading mode θ. The goal is to recover numerically a nucleation surface performing numerical tests for different θ. We focus on the set of loading directions $\theta \in [0, \pi/2]$, varying between isotropic expansion ($\theta = 0$) and pure shear ($\theta = \pi/2$), passing through uniaxial traction ($\theta = \pi/4$). We refrain from considering *compressive* stress states for which there are

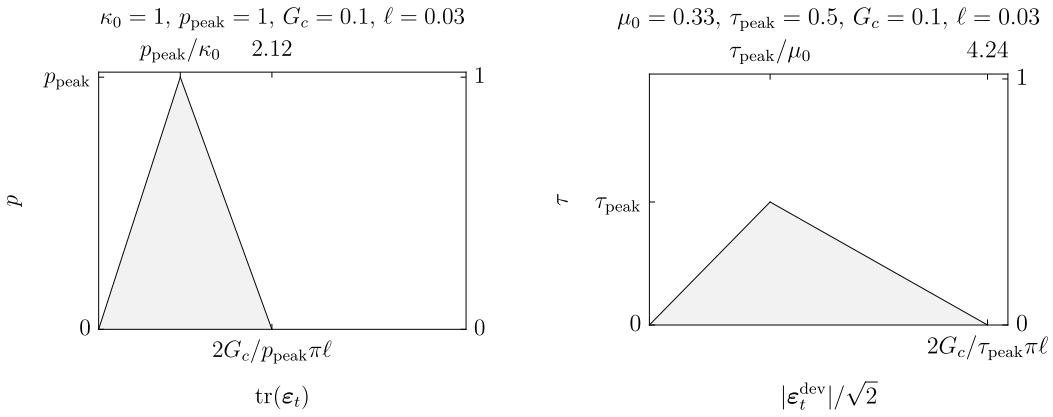

Figure 11: Homogeneous response in purely spherical (left, $\theta = 0$) and deviatoric (right, $\theta = \pi/2$) loading modes for $G_c = 0.1$, $\ell = 0.03$, $\kappa_0 = 1$, $\mu_0 = 1/3$, $p_{\text{peak}} = 1.0$, $\tau_{\text{peak}} = 0.5$. The gray area under the stress curve is the dissipated energy in a homogeneous damage process $w_1 = \frac{G_c}{\pi\ell}$ and must coincide for the two loading modes.

additional model-dependent issues, discussed in length in (Vicentini et al., 2024; Lorenzis and Maurini, 2021).

For the considered model, the peak stress surface in the stress space $\partial\mathcal{R}^*(0)$ coincides with the elastic limit. The corresponding peak surface in the strain space is $\partial\mathcal{R}(0)$. For $\text{tr}(\boldsymbol{\varepsilon}) > 0$, they are semi-ellipses with semi-axes p_{peak} and τ_{peak} for the stress and p_{peak}/κ_0 and τ_{peak}/μ_0 for the strain, see (25)-(26). The purpose of this test is to determine whether these peak loads correspond to the critical surface where damage localizes into bands to form cracks.

We set $\kappa_0 = 1$, $\mu_0 = 1/3$, $G_c = 0.1$, and $\tau_{\text{peak}} = 1/2$. To show the influence of the peak stress ratios, we perform simulations for either $p_{\text{peak}} = 1$ or $p_{\text{peak}} = 1/2$. The cohesive length-scales of the spherical and deviatoric modes are $\ell_{\text{ch}}^{(\mu)} := 2\mu_0 G_c/\tau_{\text{peak}}^2 \simeq 0.267$ and $\ell_{\text{ch}}^{(\kappa)} := 2\kappa_0 G_c/p_{\text{peak}}^2 = \{0.2, 0.8\}$. Naively extrapolating the 1d results to the multi-axial setting, we set $\ell = 0.03$ with $D = 1$ to ensure a snap-back at the peak stress. Indeed, the model verifies the strain hardening condition (30) and the condition $\pi\ell < \ell_{\text{ch}}^{(\kappa,\mu)} < D$. In 1d, this condition ensures the presence of localized solutions with snap-back at the peak load and that the homogeneous solution is always incrementally unstable. In other words, in a 1d context, these parameters would assure a "brittle" behavior with a crack appearing instantaneously at the peak load, as for the "long bar" in Figure 7a.

We discretize the problem in space with standard triangular finite elements and piecewise linear approximation using an unstructured mesh with average size $h = \ell/5$. We solve the first-order stability conditions at each time step t to find the solution with an alternate minimimization algorithm implemented in `FEniCSx` (Dokken et al., 2023). At each time step, we check numerically the second order stability of the solution using the algorithm presented in León Baldelli and Maurini (2021).We impose Dirichlet boundary conditions on $\alpha = 0$ on the whole boundary of the disk to exclude localized solutions on the boundary.

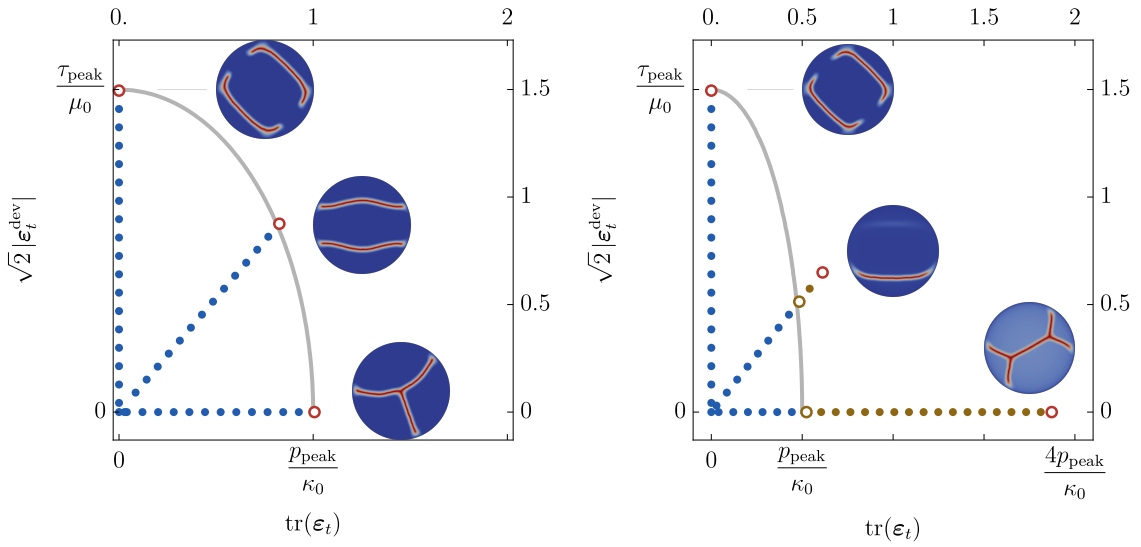

Figure 12: Multi-axial nucleation test: numerical results for different loading modes with the boundary condition (44) and $G_c = 0.1$, $\ell = 0.03$, $\kappa_0 = 1$ $\mu_0 = 1/3$. Left: $\tau_{\text{peak}} = 1/2$ and $p_{\text{peak}} = 1$. Right: $\tau_{\text{peak}} = 1/2$ and $p_{\text{peak}} = 1/2$. Each figure reports three sets of simulations obtained by increasing the loading amplitude t for loading modes that are purely isotropic ($\theta = 0$), uniaxial ($\theta = \pi/4$), and purely deviatoric ($\theta = \pi/2$). The blues dots denote solutions with null damage while the brown dots indicate solutions with diffused non-vanishing damage. The red circles mark the critical load for which damage field localizes in the form of cracks. The gray solid line represents the elastic limit in strain and the peak strain surface. The insets show the damage field on the disk immediately after the nucleation event.

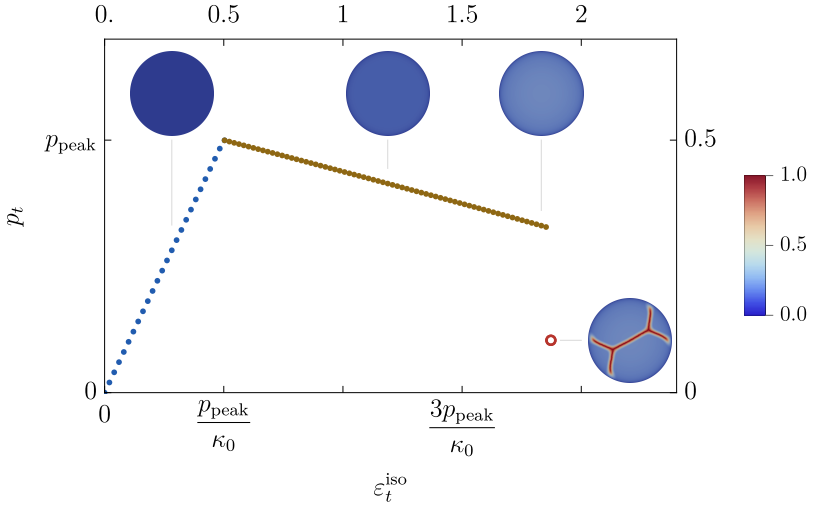

Figure 13: Global response for the purely isotropic loading mode ($\theta = 0$) reporting the pressure $p_t = \text{tr}(\boldsymbol{\sigma}_t)/2$ versus $\varepsilon_t^{\text{iso}} = \text{tr}(\boldsymbol{\varepsilon}_t)$ for the numerical parameters as in Figure 12-right ($p_{\text{peak}} = \tau_{\text{peak}} = 1/2$). The insets show the damage field on the disk at different loading level.

Figure 12 shows the results for purely isotropic loading ($\theta = 0$), uniaxial strain ($\theta = \pi/4$), and purely deviatoric loading ($\theta = \pi/2$), respectively. The gray solid line represents the elastic limit in strain given by (25) and the dots the numerical results, with elastic states

with zero damage in blue and states with diffuse non-vanishing damage in brown. The red circles mark the states corresponding to the damage localizations in the form of cracks. For $p_{\text{peak}} = 1$ (left panel) the critical load for crack nucleation coincides with the elastic limit for all the considered loading modes, as one would naively expect extrapolating the 1d results to the multiaxial setting (Figure 12-left). For $p_{\text{peak}} = 1/2$ (right panel) the crack nucleates immediately after the elastic limit for purely deviatoric loading. However, for purely isotropic and uniaxial loading modes, we observe the persistence of solution with diffuse damage after the elastic limit (Figure 12-right). For isotropic and mixed loadings, the solutions with damage localization in the form of cracks appear only for larger values of the loading parameter t, after the development of a phase with diffuse damage. To better understand this behavior, we report in Figure 13 the global response for the purely isotropic loading mode. The insets show the damage field at different loading levels.

The outcome of the simulations is somehow unexpected. It shows that the results of the 1d analysis of Section 3 cannot be directly transposed to multi-axial stress states. The current literature identifies the critical loading for crack nucleation, *i.e.* the strength, with the peak stress surface (see *e.g.* Tanné et al., 2018; Kumar et al., 2020; Lorenzis and Maurini, 2021). In the example of Figure 12, decreasing the peak stress p_{peak} from 1 to 1/2 one would expect the critical displacement loading for purely isotropic mode decreasing according. Vice versa, the numerical results show an increasing of the critical load from 1.0 to 1.87. A second-order stability analysis is necessary to get a finer understanding of the crack nucleation threshold.

4.3. Stability of states under multi-axial loading

To study the stability of the homogeneous states under multi-axial loading, we leverage the results of Pham and Marigo (2013a). To simplify the presentation, we focus on the case $\text{tr}(\boldsymbol{\varepsilon}) > 0$, assuming $\text{tr}(\boldsymbol{\varepsilon}) = \text{tr}^+(\boldsymbol{\varepsilon})$ and $\text{tr}^-(\boldsymbol{\varepsilon}) = 0$ in (46).

As discussed in Section 2.2, purely elastic solutions are stable because the damage criterion is verified as a strict inequality and the first derivative of the energy is non-negative for any non-vanishing perturbation. For damaging states, the damage criterion is verified as an equality and the first derivative of the energy is vanishing. The sign of the second derivative of the energy determines the sign of the energy increment, according to the second-order condition (18)-(22) for state and incremental stability, respectively.

For the model at hand, the second derivative of the energy in the direction $(\mathbf{v}, \beta)$ can be expressed as

$$\mathcal{E}''(\mathbf{u}_t, \alpha_t)(\mathbf{v}, \beta) = \mathcal{P}(\mathbf{u}_t, \alpha_t)(\mathbf{v}, \beta) - \mathcal{Q}(\mathbf{u}_t, \alpha_t)(\mathbf{v}, \beta) \tag{51}$$

where $\mathcal{P}(\mathbf{u}_t, \alpha_t)(\mathbf{v}, \beta)$ and $\mathcal{Q}(\mathbf{u}_t, \alpha_t)(\mathbf{v}, \beta)$ are two quadratic forms of the variations $(\mathbf{v}, \beta)$, which, for homogeneous states, are given by

$$\begin{aligned}
\mathcal{P}(\mathbf{u}_t, \alpha_t)(\mathbf{v}, \beta) &= \left(2w_1\ell^2 \int_\Omega \nabla\beta \cdot \nabla\beta dx + \int_\Omega \mathsf{A}_t \left(\boldsymbol{\varepsilon}(\boldsymbol{v}) - \beta \mathsf{S}_t' \boldsymbol{\sigma}_t\right) \cdot \left(\boldsymbol{\varepsilon}(\boldsymbol{v}) - \beta \mathsf{S}_t' \boldsymbol{\sigma}_t\right) dx \right) \\
\mathcal{Q}(\mathbf{u}_t, \alpha_t)(\mathbf{v}, \beta) &= \left(\frac{1}{2} \mathsf{S}_t'' \boldsymbol{\sigma}_t \cdot \boldsymbol{\sigma}_t - w_1 w''(\alpha_t) \right) \int_\Omega \beta^2 dx.
\end{aligned}$$

To condense the notation and render the presentation more general and consistent with Pham and Marigo (2013a), we introduce the forth-order tensors $\mathsf{A}_t := \mathsf{A}(\alpha_t)$ and $\mathsf{S}_t := \mathsf{S}(\alpha_t)$ representing the elastic stiffness and compliance. They are defined by

$$\boldsymbol{\sigma}_t = \mathsf{A}_t \boldsymbol{\varepsilon}_t = \kappa(\alpha_t) \text{tr}(\boldsymbol{\varepsilon}_t)\, I + 2\mu(\alpha_t)\, \boldsymbol{\varepsilon}_t^{\text{dev}}, \quad \mathsf{S}_t := \mathsf{A}_t^{-1}$$

with the shorthand notation $\mathsf{A}_t' := \frac{d\mathsf{A}(\alpha_t)}{d\alpha_t}$, $\mathsf{A}_t'' := \frac{d^2\mathsf{A}(\alpha_t)}{d^2\alpha_t}$, $\mathsf{S}_t' := \frac{d\mathsf{S}(\alpha_t)}{d\alpha_t}$, $\mathsf{S}_t'' := \frac{d^2\mathsf{S}(\alpha_t)}{d^2\alpha_t}$.

The first quadratic form $\mathcal{P}$ is positive semi-definite for any non-vanishing perturbation $(\mathbf{v}, \beta)$. The quadratic form $\mathcal{Q}$ is positive for stress-softening regimes and negative for strain-hardening regimes, because the sign of its first factor is determined by the sign of the derivative of the admissible stress domain (24b). This implies the response would be always stable in stress-hardening regimes. However, the model considered here is stress-softening for any non-vanishing damage level. Hence, the sign second derivative of the energy in the direction $(\mathbf{v}, \beta)$ depends on the Rayleigh ratio between the two quadratic forms $\mathcal{P}$ and $\mathcal{Q}$, that writes as

$$\mathcal{R}_L(\boldsymbol{v}, \beta) := \frac{2w_1 \frac{\ell^2}{L^2} \int_{\Omega_1} \nabla\beta \cdot \nabla\beta dy + \int_{\Omega_1} \mathsf{A}_t \left(\boldsymbol{\varepsilon}(\boldsymbol{v}) - \beta \mathsf{S}_t' \boldsymbol{\sigma}_t\right) \cdot \left(\boldsymbol{\varepsilon}(\boldsymbol{v}) - \beta \mathsf{S}_t' \boldsymbol{\sigma}_t\right) dy}{\left(\frac{1}{2}\mathsf{S}_t'' \boldsymbol{\sigma}_t \cdot \boldsymbol{\sigma}_t - w_1 w''(\alpha_t)\right) \int_{\Omega_1} \beta^2 dy}. \tag{52}$$

To render the structural scale effect explicit, we introduced the change of variable $\mathbf{x} \to \mathbf{y} := \mathbf{x}/L$, with $L = |\Omega|$, that transforms the domain Ω in Ω_1 with $|\Omega_1| = 1$. The second directional derivative is positive for $\mathcal{R}_L > 1$ and negative for $\mathcal{R}_L < 1$. Hence, according to the definition (10), the state $(\mathbf{u}_t, \alpha_t)$ is state-stable if

$$\rho_L := \min_{(\boldsymbol{v},\beta)\in\mathcal{N}_0^+} \mathcal{R}_L(\boldsymbol{v}, \beta) > 1 \tag{53}$$

and state-unstable if $\rho_L < 1$, where $\mathcal{N}_0^+$ is the set of non-vanishing perturbations defined in (17). The incremental-stability condition is tested by replacing the cone $\mathcal{N}_0^+$ with the vector space $\mathcal{N}_0$. Pham and Marigo (2013a) showed that the minimization problem is well-posed and that ρ_L exists and is positive. Adapting their results to the model and the nucleation test at hand, we obtain the following results :

- For sufficient small structures, the solution is always state-stable for any multi-axial stress states; this is because of the term in ℓ^2/L^2 in the numerator of the Rayleigh ratio (52).

- For sufficiently large structure, the stability is determined by

$$\rho_\infty := \lim_{L\to\infty} \rho_L. \tag{54}$$

  If $\rho_\infty > 1$, the solution is state-stable, independently of the structural size. If $\rho_\infty < 1$ there is a critical domain size L_c such that the solution is state-unstable for $L > L_c$ and stable for $L < L_c$.

Pham and Marigo showed also that the stability condition $\rho_\infty > 1$ for large structures coincides with the strong ellipticity condition (Ball, 1980; Benallal et al., 1993) of the underlying local damage model (see Pham and Marigo, 2013a, sec. 6).

After some calculations reported in Appendix A, we computed explicitly the value of ρ_∞ founding that the results critically depends on the load multi-axiality:

- For $\varepsilon_t^{\text{iso}} \frac{\kappa'(\alpha_t)}{\kappa(\alpha_t)} \geq \varepsilon_t^{\text{dev}} \frac{\mu'(\alpha_t)}{\mu(\alpha_t)}$,

$$\rho_\infty = 0.$$

  .

- For $\varepsilon_t^{\text{iso}} \frac{\kappa'(\alpha_t)}{\kappa(\alpha_t)} < \varepsilon_t^{\text{dev}} \frac{\mu'(\alpha_t)}{\mu(\alpha_t)}$,

$$\rho_\infty = \frac{\left(\varepsilon_t^{\text{dev}} \frac{\mu'(\alpha_t)}{\mu(\alpha_t)} - \varepsilon_t^{\text{iso}} \frac{\kappa'(\alpha_t)}{\kappa(\alpha_t)}\right)^2 \frac{\kappa(\alpha_t)\mu(\alpha_t)}{\kappa(\alpha_t)+\mu(\alpha_t)}}{\left(\varepsilon_t^{\text{iso}}\right)^2 \left(\frac{\kappa'(\alpha_t)^2}{\kappa(\alpha_t)} - \frac{\kappa''(\alpha_t)}{2}\right) + \left(\varepsilon_t^{\text{dev}}\right)^2 \left(\frac{\mu'(\alpha_t)^2}{\mu(\alpha_t)} - \frac{\mu''(\alpha_t)}{2}\right) - w_1 w''(\alpha_t)}. \tag{55}$$

This results implies that, in the former case, the homogeneous states will be always unstable for sufficiently large structure ($L \to \infty$), as in the 1d traction problem of Section 3. Vice versa, in the latter case, depending on the material parameters and the damage level, the homogeneous states can be stable in the softening regime even for infinitely large structures, which is not possible in 1d.

To test the stability criterion above, we replicate the numerical experiments on the disk for a larger number of loading modes θ. In this case, we leave the damage free on the boundary. The results are reported in Figure 14. Each red empty dot is the result of the multi-axial nucleation test for a different loading mode θ and represents the critical loading at which the homogeneous solution is incrementally-unstable numerically, according to the numerical second-order stability test. The solid gray line represents the peak strain surface, whilst the dashed red curve corresponds to the analytical second-order stability threshold, obtained as the peak strain surface where $\rho_\infty < 1$ and the region where $\rho_\infty = 1$, otherwise. The agreement between the numerical and the analytical stability results is good, even if the numerical computations tests only the incrementally stability (22) of the solution for a finite structure, whilst the analytical calculations are performed in the limit of an infinite structure and test the state-stability (18) of the solution. These results rationalize the unexpected numerical observations in Figure 12, disclosing the complex behavior of the critical surface for crack nucleation under multi-axial loading.

Even for infinitely large structure, the critical surface for crack nucleation is not always the peak stress surface, as one would naively expect. The results of the one-dimensional stability analysis cannot be extrapolated to the multidimensional case. States with dominant isotropic loading can be stable even in the softening regime and for infinitely large structures. This is because of compatibility issues arising to develop localized solution under multi-axial loading. As detailed in Pham and Marigo (2013a), these issues do not arise for rank-one states, as purely deviatoric modes.

The case of the purely isotropic loading mode is particularly interesting and can be treated analytically. The critical loading t_s for the instability of the homogeneous solution, *i.e.* for which $\rho_\infty = 1$, is computed to get

$$t_{\rm s} = \gamma_\kappa \frac{1 + \frac{\kappa_0}{\mu_0}\frac{\gamma_\mu - \gamma_\kappa}{\gamma_\kappa(\gamma_\kappa - 1)}}{1 + \frac{\kappa_0}{\mu_0}\frac{\gamma_\mu - 1}{\gamma_\kappa - 1}}\, t_{\rm peak}, \tag{56}$$

where $t_{\rm peak} = p_{\rm peak}/\kappa_0$ and $t_{\rm s} = t_{\rm peak}$ for $\gamma_\kappa = 1 + \frac{\kappa_0}{\mu_0}$. Hence, the qualitative behavior of the multiaxial stability diagram is of the type of Figure 14-left when $t_{\rm s} \le t_{\rm peak}$, *i.e.*

$$\gamma_\kappa \le 1 + \frac{\kappa_0}{\mu_0} \qquad \Leftrightarrow \qquad p_{\rm peak}^2 \ge \frac{2G_c}{\pi\ell}\frac{\kappa_0\mu_0}{\kappa_0 + \mu_0} = \gamma_\mu \frac{\tau_{\rm peak}^2}{1 + \frac{\mu_0}{\kappa_0}} \tag{57}$$

and of the type of Figure 14-right otherwise.

The condition (57) is of practical relevance when considering the setting of the parameters of the model (46) to control the critical surface for crack nucleation. The `S-LS` model allows for the independent setting of the peak stresses $p_{\rm peak}$ and $\tau_{\rm peak}$, the toughness G_c, and the stiffnesses κ_0 and μ_0, by the tuning of the parameters γ_κ and γ_μ as in (29). However, for a hard loading device, the solution becomes unstable at the peak loads only if the condition (57) is met. This implies that the ratio between the peak stresses $\tau_{\rm peak}$ and $p_{\rm peak}$ cannot be arbitrary large, being bounded by $\sqrt{1 + \mu_0/\kappa_0}$. Otherwise, the critical surface for crack nucleation will not coincide with the peak stress surface and stable homogeneous states are to be expected even after the peak load.

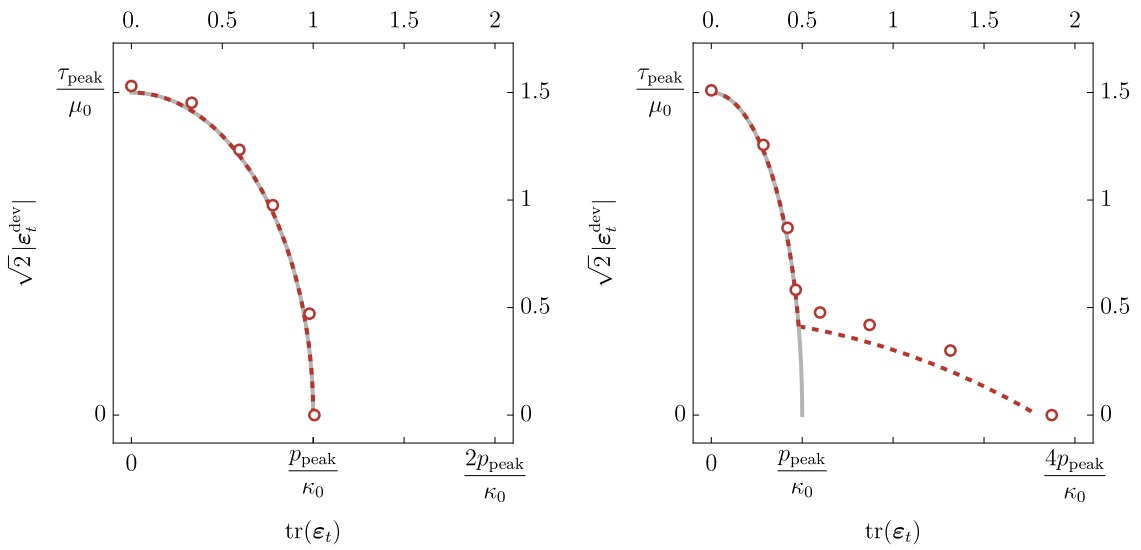

Figure 14: Multi-axial stability test of homogeneous states for $\tau_{\text{peak}} = p_{\text{peak}} = 1/2$ (left) and $\tau_{\text{peak}} = 1/2$, $p_{\text{peak}} = 1$ (right). The numerical parameters are as in Figure 12. Each red empty dot is the result of the multi-axial nucleation test for a specific θ and represents the loading for which the homogeneous solution is incrementally-unstable numerically. The gray solid line is the peak strain surface corresponding to the elastic limit. The red dashed line is the critical strain surface computed as the peak strain surface where $\rho_\infty < 1$ and the region where $\rho_\infty = 1$, otherwise.

5. Conclusion

In variational phase-field models of fracture, cracks nucleate when solutions with diffuse damage become unstable and damage localizes in crack-like bands. In the literature, nucleation is assumed to take place at the peak stress, associated to the transitions from stress-hardening to stress-softening behavior. We have shown that the conditions for the loss of stability of the homogeneous solution and crack nucleation are more complex and subtler. Our results provide a theoretical and numerical methodological framework to rationalize the complex crack nucleation conditions observed in numerical simulations.

To conduct this analysis, we considered the model introduced by Alessi et al. (2014a), which represents a minor modification of the cohesive-like by Lorentz et al. (2011). As a main advantage, it enables a complete analytical derivation of homogeneous and localized solutions in 1d. This model features a softening parameter γ, which allows for the independent adjustment of G_c and σ_{peak}, regardless of the regularization length ℓ, provided that the latter is taken sufficiently small, see (30).

We considered first the elemental one-dimensional traction problem. The analytical solutions and the second-order stability analysis disclosed the fundamental role played by the Irwin length $\ell_{\text{ch}} = E_0 G_c/\sigma_{\text{peak}}^2$ in characterizing the behavior of the structure:

- If $\ell_{\text{ch}} < L$ (large structures), the homogeneous solution is state-unstable and all the possible localized solutions show snap-back. This means that in a displacement-controlled tensile test (hard-device), once the peak stress is reached, the solution brutally snaps from a completely elastic state to a fully localized solution with $\alpha_{\max} = 1$. We define this behavior as *brittle*.

- If $\pi\ell < L < \ell_{\text{ch}}$ (small structure), the homogeneous solution is state-stable but incrementally-

unstable. This complex scenario implies that the homogeneous solution is observable but not unique, being in competition with localized solutions with similar energies. The localized solutions do not present snap-back at the peak load and may evolve with a stable evolution. The evolution of the localised damage field in a displacement-controlled tensile test evolves smoothly. We classify this behavior as strongly *cohesive*.

The ratio $\ell_{\rm ch}/L = 2E_0G_c/(\sigma^2_{\rm peak}L)$ measures the competition of the energy dissipated to form a unit surface crack, G_c, and the stored elastic energy at the peak stress, $\sigma^2_{\rm peak}L/(2E_0)$. If the latter is large enough to pay-off the energetic price G_c of a crack, the model shows a brittle behavior. In very stiff bars, the stored elastic energy is very low. This explains why the brittle failure of nearly inextensible bars under displacement control is not possible with the considered models. The modification of the model introducing a more complex nonlinear constitutive behavior with reduction of the stiffness before failure may be necessary to account for the experimental results. This is the object of an ongoing research, not reported here.

In the multi-dimensional model, we introduced two softening parameters, γ_κ and γ_μ modulating independently the softening behavior of purely deviatoric and volumetric states, respectively. Nominally, they allow for the independent adjustment of the peak load $p_{\rm peak}$ and $\tau_{\rm peak}$ for the spherical and the deviatoric loading modes. However, the second-order stability discloses new effects, absent in the 1d traction problem. In the multi-dimensional case, the nucleation behavior under displacement-controlled purely deviatoric states is different from the one under displacement-controlled purely spherical states. We showed that, while deviatoric states are always unstable for sufficiently large structures, spherical states tends to be stable even in the softening regime and for infinitely large structures. Hence, even for infinitely large structures, the critical surface for crack nucleation is not always the peak stress surface, as one would naively expect. The results of the one-dimensional stability analysis cannot be extrapolated to the multidimensional case. This effect limits flexibility in setting $p_{\rm peak}$ and $\tau_{\rm peak}$ because they do not always correspond to critical loads if the ratio $\tau_{\rm peak}/p_{\rm peak}$ is too large, see equation (57).

Acknowledgements

This research has received funding from the European Union's Horizon 2020 research and innovation programme under the Marie Skłodowska-Curie grant agreement No. 861061 – NEWFRAC Project. This work was performed using HPC resources from GENCI-IDRIS (Grant 2023-AD010913451R1)

Appendix A. Calculation of $\boldsymbol{\rho_\infty}$

Appendix A.1. General definitions

According to Lemma 1 in Pham and Marigo (2013a) ρ_∞ is given by:

$$\rho_\infty(\boldsymbol{\varepsilon}_t) = \frac{\mathsf{A}(\alpha_t)\mathsf{S}'(\alpha_t)\boldsymbol{\sigma}_t \cdot \mathsf{S}'(\alpha_t)\boldsymbol{\sigma}_t - \delta(\boldsymbol{\varepsilon}_t)}{\frac{1}{2}\mathsf{S}''(\alpha_t)\boldsymbol{\sigma}_t \cdot \boldsymbol{\sigma}_t - w_1 w''(\alpha_t)} \tag{A.1}$$

In order to define $\delta(\boldsymbol{\varepsilon}_t)$, we need to introduce some preliminary definitions.

Let $\boldsymbol{b}$ be the unit vector which defines the unit sphere $\mathbb{S}^n$ of $\mathbb{R}^n$ such that $\mathbb{S}^n = \{\boldsymbol{b} \in \mathbb{R}^n : |\boldsymbol{b}| = 1\}$. Thus, we can define the n-dimension subspace $V(\boldsymbol{b})$ of $\mathbb{M}^n_s$ by

$$V(\boldsymbol{b}) = \{\boldsymbol{b} \otimes \boldsymbol{v} + \boldsymbol{v} \otimes \boldsymbol{b} : \boldsymbol{v} \in \mathbb{R}^n\} \tag{A.2}$$

over which we can obtain $\delta(\boldsymbol{\varepsilon}_t)$ by solving the following maximization problem

$$\delta(\boldsymbol{\varepsilon}_t) = \max_{\{\boldsymbol{b}:|\boldsymbol{b}|=1\}} \mathsf{A}(\alpha_t)\boldsymbol{\xi}(\boldsymbol{b}) \cdot \boldsymbol{\xi}(\boldsymbol{b}), \tag{A.3}$$

where $\boldsymbol{\xi}(\boldsymbol{b}) \in V(\boldsymbol{b})$ is calculated as follows

$$\boldsymbol{\xi}(\boldsymbol{b}) = \underset{\boldsymbol{\xi}\in V(\boldsymbol{b})}{\arg\min}\, \mathsf{A}(\alpha_t)(\mathsf{S}'(\alpha_t)\boldsymbol{\sigma}_t - \boldsymbol{\xi}) \cdot (\mathsf{S}'(\alpha_t)\boldsymbol{\sigma}_t - \boldsymbol{\xi}). \tag{A.4}$$

Appendix A.2. ρ_∞ for 2D mixed deviatoric-volumetric homogeneous states

In order to calculate $\delta(\boldsymbol{\varepsilon}_t)$, we define the optimal vector $\boldsymbol{v}(\boldsymbol{b}) \in \mathbb{R}^n$ such that $\boldsymbol{\xi}(\boldsymbol{b}) = \boldsymbol{b} \otimes \boldsymbol{v}(\boldsymbol{b}) + \boldsymbol{v}(\boldsymbol{b}) \otimes \boldsymbol{b}$. We then insert $\boldsymbol{v}(\boldsymbol{b})$ into (A.4) in order to find the optimal $\boldsymbol{v}(\boldsymbol{b})$ and therefore $\boldsymbol{\xi}(\boldsymbol{b})$ which minimise (A.4):

$$\begin{aligned}\boldsymbol{v}(\boldsymbol{b}) = &-\frac{b_1\left[2\varepsilon_{\mathrm{dev}}\kappa(\alpha)\mu'(\alpha)b_2^2 + \frac{\mu(\alpha)}{2}(\varepsilon_{\mathrm{iso}}\kappa'(\alpha) + \varepsilon_{\mathrm{dev}}\mu'(\alpha))\right]}{\mu(\alpha)(\kappa(\alpha)+\mu(\alpha))}\boldsymbol{e}_1 \\ &+\frac{b_2\left[\varepsilon_{\mathrm{dev}}\kappa(\alpha)\mu'(\alpha)b_1^2 + \frac{\mu(\alpha)}{2}(-\varepsilon_{\mathrm{iso}}\kappa'(\alpha) + \varepsilon_{\mathrm{dev}}\mu'(\alpha))\right]}{\mu(\alpha)(\kappa(\alpha)+\mu(\alpha))}\boldsymbol{e}_2\end{aligned} \tag{A.5}$$

where b_1 and b_2 are respectively the component along $\boldsymbol{e}_1$ and $\boldsymbol{e}_2$ of the unitary vector $\boldsymbol{b}$. Then, maximizing $\mathsf{A}(\alpha_t)\boldsymbol{\xi}(\boldsymbol{b})\cdot\boldsymbol{\xi}(\boldsymbol{b})$ over all the unitary vectors $\boldsymbol{b} \in \mathbb{R}^2$, we get the following expression for $\delta(\boldsymbol{\varepsilon}_t)$:

$$\delta(\boldsymbol{\varepsilon}_t) = \begin{cases} \frac{4\varepsilon_{\mathrm{iso}}^2\kappa'(\alpha)^2}{\kappa(\alpha)} + \frac{4\varepsilon_{\mathrm{dev}}^2\mu'(\alpha)^2}{\mu(\alpha)} & \text{if } \frac{\varepsilon_{\mathrm{iso}}\mu(\alpha)\kappa'(\alpha)}{\varepsilon_{\mathrm{dev}}\kappa(\alpha)\mu'(\alpha)} \le 1 \\ \frac{4(\varepsilon_{\mathrm{iso}}\kappa'(\alpha)+\varepsilon_{\mathrm{dev}}\mu'(\alpha))^2}{\kappa(\alpha)+\mu(\alpha)} & \text{if } \frac{\varepsilon_{\mathrm{iso}}\mu(\alpha)\kappa'(\alpha)}{\varepsilon_{\mathrm{dev}}\kappa(\alpha)\mu'(\alpha)} > 1 \end{cases} \tag{A.6}$$

and applying (A.1) to our case, we finally find:

$$\rho_\infty(\boldsymbol{\varepsilon}_t) = \begin{cases} 0 & \text{if } \frac{\varepsilon_{\mathrm{iso}}\mu(\alpha)\kappa'(\alpha)}{\varepsilon_{\mathrm{dev}}\kappa(\alpha)\mu'(\alpha)} \le 1 \\ \frac{(\varepsilon_{\mathrm{dev}}\kappa(\alpha)\mu'(\alpha)-\varepsilon_{\mathrm{iso}}\mu(\alpha)\kappa'(\alpha))^2}{(\kappa(\alpha)+\mu(\alpha))\left[\mu(\alpha)\left(\kappa(\alpha)\left(\varepsilon_{\mathrm{dev}}^2\frac{\mu''(\alpha)}{2}+\varepsilon_{\mathrm{iso}}^2\frac{\kappa''(\alpha)}{2}+w_1w''(\alpha)\right)-\varepsilon_{\mathrm{iso}}^2\kappa'(\alpha)^2\right)-\varepsilon_{\mathrm{dev}}^2\kappa(\alpha)\mu'(\alpha)^2\right]} & \text{if } \frac{\varepsilon_{\mathrm{iso}}\mu(\alpha)\kappa'(\alpha)}{\varepsilon_{\mathrm{dev}}\kappa(\alpha)\mu'(\alpha)} > 1. \end{cases} \tag{A.7}$$

Appendix A.3. ρ_∞ for purely volumetric homogeneous states

With a similar procedure we used to calculate $\boldsymbol{v}(\boldsymbol{b})$ for 2D mixed deviatoric-volumetric homogeneous states and considering (5) we get

$$\boldsymbol{v}(\boldsymbol{b}) = -\frac{\kappa'(\alpha)}{\kappa(\alpha)+(n-1)^2\mu(\alpha)}\frac{\mathrm{tr}(\boldsymbol{\varepsilon}_t)}{2}\boldsymbol{b}. \tag{A.8}$$

Thus, it turns out that $\mathsf{A}(\alpha_t)\boldsymbol{\xi}(\boldsymbol{b})\cdot\boldsymbol{\xi}(\boldsymbol{b})$ is independent of $\boldsymbol{b}$, so we find the following expression for $\delta(\boldsymbol{\varepsilon}_t)$:

$$\delta(\boldsymbol{\varepsilon}_t) = \frac{\kappa'(\alpha)^2}{\kappa(\alpha)+(n-1)^2\mu(\alpha)}\mathrm{tr}(\boldsymbol{\varepsilon}_t)^2. \tag{A.9}$$

If we apply (A.1), we get

$$\rho_\infty(\boldsymbol{\varepsilon}_t) = -\frac{\mathrm{tr}(\boldsymbol{\varepsilon}_t)^2\mu(\alpha)\kappa'(\alpha)^2}{(\kappa(\alpha)+(n-1)^2\mu(\alpha))\left[\mathrm{tr}(\boldsymbol{\varepsilon}_t)^2\left(\frac{\kappa(\alpha)\kappa''(\alpha)}{n}-\frac{2k'(\alpha)^2}{n}\right)+\frac{2w_1w''(\alpha)\kappa(\alpha)}{n}\right]}. \tag{A.10}$$

Inverting the multi-dimensional damage criterion from (48) applied to a purely volumetric state we can calculate the homogeneous damage field, function of $\mathrm{tr}(\boldsymbol{\varepsilon}_t)$:

$$\alpha_t(\boldsymbol{\varepsilon}_t) = 1 - \sqrt{\frac{\gamma_\kappa - \mathrm{tr}(\boldsymbol{\varepsilon}_t)/\mathrm{tr}(\boldsymbol{\varepsilon}_{\mathrm{peak}})}{\gamma_\kappa - 1}}, \tag{A.11}$$

where $\mathrm{tr}(\boldsymbol{\varepsilon}_{\mathrm{peak}}) = \frac{p_{\mathrm{peak}}}{\kappa_0}$ is the isotropic peak strain. Hence, we can express $\rho_\infty(\boldsymbol{\varepsilon}_t)$ for the 2D case:

$$\rho_\infty(\boldsymbol{\varepsilon}_t) = \frac{2(\gamma_\kappa - 1)\gamma_\kappa(\nu_0 - 1)}{2\gamma_\kappa\left[\frac{\mathrm{tr}(\boldsymbol{\varepsilon}_t)}{\mathrm{tr}(\boldsymbol{\varepsilon}_{\mathrm{peak}})}(\nu_0 - 1) - \nu_0 - 1\right] + 4\frac{\mathrm{tr}(\boldsymbol{\varepsilon}_t)}{\mathrm{tr}(\boldsymbol{\varepsilon}_{\mathrm{peak}})} + 2\gamma_\kappa\left(\frac{\mathrm{tr}(\boldsymbol{\varepsilon}_t)}{\mathrm{tr}(\boldsymbol{\varepsilon}_{\mathrm{peak}})} - 1\right)(\nu_0 - 1)\left(\frac{p_{\mathrm{peak}}}{\tau_{\mathrm{peak}}}\right)^2}. \tag{A.12}$$

References

R. Alessi, J.-J. Marigo, and S. Vidoli. Gradient Damage Models Coupled with Plasticity and Nucleation of Cohesive Cracks. *Archive of Rational Mechanics and Analysis*, 214(2):575–615, 2014a. doi: 10.1007/s00205-014-0763-8. URL `http://link.springer.com/10.1007/s00205-014-0763-8`.

R. Alessi, M. Ambati, T. Gerasimov, S. Vidoli, and L. De Lorenzis. Comparison of phase-field models of fracture coupled with plasticity. In E. Oñate, D. Peric, E. de Souza Neto, and M. Chiumenti, editors, *Advances in Computational Plasticity: A Book in Honour of D. Roger J. Owen*, pages 1–21. Springer International Publishing, Cham, 2018. ISBN 978-3-319-60885-3.

R. Alessi, J.-J. Marigo, and S. Vidoli. Gradient Damage Models Coupled with Plasticity and Nucleation of Cohesive Cracks. *Archive of Rational Mechanics and Analysis*, 214(2):575–615, November 2014b. ISSN 1432-0673. doi: 10.1007/s00205-014-0763-8. URL `https://doi.org/10.1007/s00205-014-0763-8`.

L. Ambrosio and M. V. Tortorelli. Tortorelli, v.: On the approximation of functionals depending on jumps by elliptic functionals via γ-convergence. commun. pure appl. math. 43(8), 999-1036. *Communications on Pure and Applied Mathematics*, 43:999 – 1036, 12 1990. doi: 10.1002/cpa.3160430805.

H. Amor, J.-J. Marigo, and C. Maurini. Regularized formulation of the variational brittle fracture with unilateral contact: Numerical experiments. *Journal of the Mechanics and Physics of Solids*, 57(8):1209–1229, 2009. doi: 10.1016/j.jmps.2009.04.011.

S. Balay, S. Abhyankar, M. F. Adams, S. Benson, J. Brown, P. Brune, K. Buschelman, E. Constantinescu, L. Dalcin, A. Dener, V. Eijkhout, J. Faibussowitsch, W. D. Gropp, V. Hapla, T. Isaac, P. Jolivet, D. Karpeev, D. Kaushik, M. G. Knepley, F. Kong, S. Kruger, D. A. May, L. C. McInnes, R. T. Mills, L. Mitchell, T. Munson, J. E. Roman, K. Rupp, P. Sanan, J. Sarich, B. F. Smith, S. Zampini, H. Zhang, H. Zhang, and J. Zhang. PETSc/TAO users manual. Technical Report ANL-21/39 - Revision 3.20, Argonne National Laboratory, 2023.

J. M. Ball. Strict convexity, strong ellipticity, and regularity in the calculus of variations. 87 (3):501–513, 1980. ISSN 0305-0041, 1469-8064. doi: 10.1017/S0305004100056930.

A. Benallal, R. Billardon, and G. Geymonat. *Bifurcation and Localization in Rate-Independent Materials. Some General Considerations*, pages 1–44. Springer Vienna, Vienna, 1993. ISBN 978-3-7091-2712-4. doi: 10.1007/978-3-7091-2712-4_1.

D. Bigoni. *Nonlinear Solid Mechanics. Bifurcation Theory and Material Instability*. Cambridge University Press, 2012.

B. Bourdin, G. Francfort, and J.-J. Marigo. Numerical experiments in revisited brittle fracture. *Journal of the Mechanics and Physics of Solids*, 48:797–826, 04 2000. doi: 10.1016/S0022-5096(99)00028-9.

B. Bourdin, G. Francfort, and J.-J. Marigo. The variational approach to fracture. *Journal of Elasticity*, 91:5–148, 04 2008. doi: 10.1007/s10659-007-9107-3.

B. Bourdin, J.-J. Marigo, C. Maurini, and P. Sicsic. Morphogenesis and Propagation of Complex Cracks Induced by Thermal Shocks. *Physical Review Letters*, 112:014301, 2014. doi: 10.1103/PhysRevLett.112.014301. URL `http://link.aps.org/doi/10.1103/PhysRevLett.112.014301`.

S. Conti, M. Focardi, and F. Iurlano. Phase field approximation of cohesive fracture models. 33 (4):1033–1067, 2016. ISSN 0294-1449, 1873-1430. doi: 10.1016/j.anihpc.2015.02.001. URL `https://ems.press/doi/10.1016/j.anihpc.2015.02.001`.

S. Conti, M. Focardi, and F. Iurlano. Phase-Field Approximation of a Vectorial, Geometrically Nonlinear Cohesive Fracture Energy. 248(2):21, 2024. ISSN 0003-9527, 1432-0673. doi: 10.1007/s00205-024-01962-4. URL `https://link.springer.com/10.1007/s00205-024-01962-4`.

J. Dokken, I. Baratta, J. Dean, M. Habera, J. Hale, C. Richardson, M. Rognes, N. Sime, and G. Wells. Dolfinx: The next generation fenics problem solving environment. *Zenodo*, 12/2023 2023. doi: 10.5281/zenodo.10447666. URL `https://zenodo.org/records/10447666`.

B. Fedelich and A. Ehrlacher. An analysis of stability of equilibrium and of quasi-static transformations on the basis of the dissipation function. *European Journal of Mechanics A*, 16:833–855, 1997.

Y. Feng and J. Li. Phase-field cohesive fracture theory: A unified framework for dissipative systems based on variational inequality of virtual works. 159:104737, 2022. ISSN 00225096. doi: 10.1016/j.jmps.2021.104737. URL `https://linkinghub.elsevier.com/retrieve/pii/S0022509621003446`.

M. Frémond and B. Nedjar. Damage, gradient of damage and principle of virtual power. 33 (8):1083–1103, 1996.

A. Griffith. The phenomena of rupture and flow in solids. *Philosophical Transactions of the Royal Society A*, 221:163–198, 1921.

R. Hill. A general theory of uniqueness and stability in elastic-plastic solids. *Journal of the Mechanics and Physics of Solids*, 6(3):236 – 249, 1958.

G. Irwin. Fracture. In *Encyclopedia of Physics*, volume 6, page 55. Springer, 1958.

A. Kumar and O. Lopez-Pamies. The poker-chip experiments of Gent and Lindley (1959) explained. *Journal of the Mechanics and Physics of Solids*, 150:104359, May 2021. ISSN 00225096. doi: 10.1016/j.jmps.2021.104359.

A. Kumar, B. Bourdin, G. A. Francfort, and O. Lopez-Pamies. Revisiting nucleation in the phase-field approach to brittle fracture. *Journal of the Mechanics and Physics of Solids*, 142:104027, 2020.

C. J. Larsen. Variational phase-field fracture with controlled nucleation. 128:104059, 2023. ISSN 00936413. doi: 10.1016/j.mechrescom.2023.104059. URL https://linkinghub.elsevier.com/retrieve/pii/S0093641323000174.

A. A. León Baldelli and C. Maurini. Numerical bifurcation and stability analysis of variational gradient-damage models for phase-field fracture. *Journal of the Mechanics and Physics of Solids*, 152:104424, July 2021. ISSN 0022-5096. doi: 10.1016/j.jmps.2021.104424. URL https://www.sciencedirect.com/science/article/pii/S0022509621001010.

E. Lorentz and S. Andrieux. Analysis of non-local models through energetic formulations. 40: 2905–2936, 2003.

E. Lorentz and A. Benallal. Gradient constitutive relations: Numerical aspects and application to gradient damage. 194(50–52):5191–5220, 2005. ISSN 0045-7825. doi: http://dx.doi.org/10.1016/j.cma.2004.12.016. URL http://www.sciencedirect.com/science/article/pii/S0045782505000307.

E. Lorentz, S. Cuvilliez, and K. Kazymyrenko. Convergence of a gradient damage model toward a cohesive zone model. *Comptes Rendus Mécanique*, 339(1):20–26, 2011. ISSN 1631-0721. doi: http://dx.doi.org/10.1016/j.crme.2010.10.010. URL http://www.sciencedirect.com/science/article/pii/S1631072110001671.

E. Lorentz, S. Cuvilliez, and K. Kazymyrenko. Modelling large crack propagation: From gradient damage to cohesive zone models. *International Journal of Fracture*, 178(1-2): 85–95, 2012. ISSN 0376-9429, 1573-2673. doi: 10.1007/s10704-012-9746-7. URL http://link.springer.com/10.1007/s10704-012-9746-7.

L. D. Lorenzis and C. Maurini. Nucleation under multi-axial loading in variational phase-field models of brittle fracture. *International Journal of Fracture*, 2021. ISSN 1573-2673. doi: 10.1007/s10704-021-00555-6. URL https://doi.org/10.1007/s10704-021-00555-6.

J.-J. Marigo, C. Maurini, and K. Pham. An overview of the modelling of fracture by gradient damage models. *Meccanica*, 51(12):3107–3128, 12 2016. ISSN 1572-9648. doi: 10.1007/s11012-016-0538-4. URL https://doi.org/10.1007/s11012-016-0538-4.

A. Mielke. Evolution of rate-indipendent system. In C. Dafermos and E. Feireisl, editors, *Handbook of Differential Equations, Evolutionary Equations*, volume 2, chapter 6, pages 461–559. Elsevier, 2005.

Q. S. Nguyen. *Bifurcation and Stability of Time-Independent Standard Dissipative Systems*, pages 45–94. Springer Vienna, Vienna, 1993. ISBN 978-3-7091-2712-4. doi: 10.1007/978-3-7091-2712-4_2. URL https://doi.org/10.1007/978-3-7091-2712-4_2.

S. Q. Nguyen and N. Triantafyllidis. Plastic bifurcation and postbifurcation analysis for generalized standard continua. *Journal of the Mechanics and Physics of Solids*, 37(5):545–566, 1989. ISSN 0022-5096. doi: http://dx.doi.org/10.1016/0022-5096(89)90028-8.

H. Petryk. *Theory of Bifurcation and Instability in Time-Independent Plasticity*, pages 95–152. Springer Vienna, Vienna, 1993. ISBN 978-3-7091-2712-4. doi: 10.1007/978-3-7091-2712-4_3. URL https://doi.org/10.1007/978-3-7091-2712-4_3.

K. Pham and J.-J. Marigo. Stability of Homogeneous States with Gradient Damage Models: Size Effects and Shape Effects in the Three-Dimensional Setting. *J Elast*, 110(1):63–93, January 2013a. ISSN 1573-2681. doi: 10.1007/s10659-012-9382-5. URL https://doi.org/10.1007/s10659-012-9382-5.

K. Pham, J.-J. Marigo, and C. Maurini. The issues of the uniqueness and the stability of the homogeneous response in uniaxial tests with gradient damage models. *Journal of the Mechanics and Physics of Solids*, 59(6):1163–1190, 2011a. doi: 10.1016/j.jmps.2011.03.010.

K. Pham and J.-J. Marigo. From the onset of damage to rupture: construction of responses with damage localization for a general class of gradient damage models. *Continuum Mechanics and Thermodynamics*, 25(2-4):147–171, 2013b. doi: 10.1007/s00161-011-0228-3. URL https://hal.archives-ouvertes.fr/hal-00647860. Publisher: Springer Verlag.

K. Pham, H. Amor, J.-J. Marigo, and C. Maurini. Gradient Damage Models and Their Use to Approximate Brittle Fracture. *International Journal of Damage Mechanics*, 20(4):618–652, May 2011b. ISSN 1056-7895, 1530-7921. doi: 10.1177/1056789510386852. URL http://journals.sagepub.com/doi/10.1177/1056789510386852.

M. Potier-Ferry. Towards a catastrophe theory for the mechanics of plasticity and fracture. *International Journal of Engineering Science*, 23(8):821 – 837, 1985.

P. Sicsic, J.-J. Marigo, and C. Maurini. Initiation of a periodic array of cracks in the thermal shock problem: A gradient damage modeling. *Journal of the Mechanics and Physics of Solids*, 63(0):256–284, 2014. ISSN 0022-5096. doi: 10.1016/j.jmps.2013.09.003. URL http://www.sciencedirect.com/science/article/pii/S0022509613001786.

B. Talamini, M. R. Tupek, A. J. Stershic, T. Hu, J. W. Foulk, J. T. Ostien, and J. E. Dolbow. Attaining regularization length insensitivity in phase-field models of ductile failure. *Computer Methods in Applied Mechanics and Engineering*, 384:113936, 2021.

E. Tanné, T. Li, B. Bourdin, J.-J. Marigo, and C. Maurini. Crack nucleation in variational phase-field models of brittle fracture. *Journal of the Mechanics and Physics of Solids*, 110:80–99, 2018. ISSN 0022-5096. doi: 10.1016/j.jmps.2017.09.006. URL http://www.sciencedirect.com/science/article/pii/S0022509617306543.

F. Vicentini, C. Zolesi, P. Carrara, C. Maurini, and L. De Lorenzis. On the energy decomposition in variational phase-field models for brittle fracture under multi-axial stress states. *International Journal of Fracture*, 2024. doi: 10.1007/s10704-024-00763-w.

J.-Y. Wu and V. P. Nguyen. A length scale insensitive phase-field damage model for brittle fracture. *Journal of the Mechanics and Physics of Solids*, 119:20–42, October 2018. ISSN 0022-5096. doi: 10.1016/j.jmps.2018.06.006. URL https://www.sciencedirect.com/science/article/pii/S0022509618302643.